

1 **Debris cover effects on energy and mass balance of Batura Glacier in the Karakoram over the**
2 **past 20 years**

3 Yu Zhu^{1,2}, Shiyin Liu^{1,2,5*}, Ben W. Brock³, Lide Tian^{1,2}, Ying Yi^{1,2}, Fuming Xie^{1,2}, Donghui Shangguan⁴, and
4 YiYuan Shen^{1,2}

5 ¹ Yunnan Key Laboratory of International Rivers and Transboundary Eco-security, 650091 Kunming, China

6 ² Institute of International Rivers and Eco-Security, Yunnan University, 650091 Kunming, China

7 ³ Department of Geography and Environmental Sciences, Northumbria University, Newcastle upon Tyne, NE1 8ST,
8 UK

9 ⁴ Northwest Institute of Eco-Environment and Resources, Chinese Academy of Sciences, Lanzhou 730000, China

10 ⁵ International Joint Laboratory of China-Laos-Bangladesh-Myanmar Natural Resources Remote Sensing
11 Monitoring

12

13 Corresponding author: Shiyin Liu (shiyin.liu@ynu.edu.cn)

14

15 Abstract:

16 The influence of supraglacial debris cover on ~~glacier mass balance~~~~glacier dynamics~~ in the Karakoram is noteworthy.
17 However, understanding of how debris cover affects the seasonal and long-term variations in glacier mass balance
18 through alterations in the glacier's energy budget is incomplete. The present study ~~applied~~~~coupled~~ an energy-mass
19 balance model ~~coupling with~~ heat conduction within debris layers on debris-covered Batura Glacier in Hunza valley,
20 to demonstrate the influence of debris cover on glacial surface energy and mass exchanges during 2000-2020. The
21 mass balance of Batura Glacier is estimated to be -0.262 ± 0.561 m w.e. yr⁻¹, with debris cover ~~reduced~~~~accounting~~
22 ~~for a 45% reduction in~~of the negative mass balance. Due to the presence of debris cover, a significant portion of
23 incoming energy is utilized for heating debris, leading to a large energy emission to atmosphere via thermal radiation
24 and turbulent sensible heat. This, in turn, ~~reduces~~ the melt latent heat ~~energy~~ at the glacier surface. We found that
25 the mass balance exhibits a pronounced arch-shaped structure along the elevation gradient, which ~~is associated~~
26 ~~with primarily attributes to~~ the distribution of debris thickness and the ~~increasing~~ impact of debris cover on the
27 energy budget ~~within various~~~~with decreasing~~ elevation ~~zones~~. Through a comprehensive analysis of the energy
28 transfer within each debris layer, we have demonstrated that the primary impact of debris cover lies in its ability to
29 modify the energy flux reaching the surface of the glacier. Thicker debris cover results in a smaller temperature
30 ~~gradient~~~~contrast between~~~~within~~ debris layers, ~~and the ice contact zone~~, consequently reducing ~~heat~~
31 ~~conduction~~~~energy reaching~~ the debris-ice interface. ~~Over the past two decades, Batura Glacier exhibited a trend~~
32 ~~toward less negative mass balance, likely linked to a decrease in air temperature and reduced ablation in areas with~~

~~thin or sparse debris cover. Over the past two decades. The glacier exhibits a tendency towards a smaller negative mass balance, with diminishing dominance of ablation in areas with thin debris cover and debris-free parts of the ablation area.~~

1 Introduction

Karakoram Glaciers have maintained a relative stable status under atmospheric warming, compared with other High Mountain Asia (HMA) glaciers over past 30 years (Zemp et al., 2019; Nie et al., 2021; Gardelle et al., 2012), a phenomenon which has been referred to as the “Karakoram Anomaly” (Hewitt, 2005). However, due to the influence of topographical and supraglacial features, the rate of glacier change across this region exhibits a distinct spatial heterogeneity. Notably, supraglacial debris plays a key role in mass change on many ~~covered~~ glaciers in the Karakoram. Over the past three decades, a discernible expansion of supraglacial debris has been observed throughout the Karakoram region (Xie et al., 2023), achieving a notable coverage of 21% in ~~select~~ areas such as the Hunza river basin (Xie et al., 2020). Ever since Hewitt (2005) identified the inhibitory effect of supraglacial debris on melt, particularly below 3500m, as a possible explanation for the “Karakoram Anomaly”, mapping the changes in the extent and mass changes of debris-covered glaciers has been the focus of several recent studies (e.g., Mölg et al. (2018), Azam et al. (2018), Xie et al. (2020)).

Until now, the direct assessment of debris impact on Karakoram glaciers has been limited to a few glaciological measurements conducted over short periods. Mihalcea et al. (2008) modeled debris-covered ice ablation across the ablation area of the Baltoro glacier, employing a distributed approach that calculated conductive heat flux through the debris layer. However, their study lacked a thorough ~~discussion-analysis of~~ the debris effect on ice melt. Recently, Huo et al. (2021) conducted advanced research on the Baltoro glacier, presenting a model that comprehensively characterizes ablation dynamics, considering temporally-linked radiative forcing, surface geomorphological evolution, and gravitational debris flux. They emphasized the role of system couplings and feedbacks between surface morphology, melt, and debris transport, revealing an overall increase in ablation due to high-frequency topographic variations leading to a larger area with thin debris cover. At a larger scale, such as the Central Karakoram, Minora et al. (2015) reported a noticeable difference in melt rates between debris-covered and debris-free ice, utilizing an enhanced temperature index model. Furthermore, by conducting ~~a comparative~~ modelling study of ice melt with and without debris cover ~~on glacier~~ for one ablation season in 2004, Collier et al. (2015) ~~found-estimated~~ that debris cover reduced ablation by approximately 14% ~~of ablation~~ in the Karakoram.

62 They attributed this significant reduction to ~~melt-rates~~insulation by ~~under-thicker~~ debris cover compensating
63 for exceeding increases in melt under ~~thinner~~ debris. Additionally, Groos et al. (2017) confirmed that debris
64 influences the ~~anomaly~~anomalous behavior of glaciers in the Karakoram using a surface mass balance model. They
65 emphasized that debris is not the sole driver, however; factors such as favorable meteorological conditions and the
66 timing of the main precipitation season also contribute. Consequently, the distribution of debris holds strong
67 potential for affecting atmosphere–glacier feedbacks and glacier ablation in this region, warranting more
68 comprehensive exploration of the intricate dynamics of mass and heat exchange within the debris in the Karakoram.

69 Supraglacial debris up to a few centimeters thickness generally increases melt due to lowered albedo and
70 increased heat absorption at the surface (Collier et al., 2014), while thicker debris cover ~~can~~typically ~~suppresses~~
71 the melt rate through insulation (Østrem, 1959; Nicholson and Benn, 2006; Bisset et al., 2020). These contrasting
72 effects have been demonstrated by many recent studies (Gardelle et al., 2012; Nuimura et al., 2017; Basnett et al.,
73 2013; Fujita and Sakai, 2014). The reduction of ablation associated with increasing debris thickness down glacier
74 can lead to an inverted mass-balance elevation profile on the debris-covered ablation zone, which has profound
75 implications on the evolution of a glacier under a warming climate (Banerjee, 2017). Some field studies have also
76 identified diverse effects on melt rates of debris cover with different thickness in Karakoram; ~~one~~ particular finding
77 showed that thin debris cover, e.g. 0.5 cm in thickness, does not accelerate ice melting in this region (Muhammad
78 et al., 2020). However, some remote sensing based research proposed that while thick debris typically inhibits the
79 melt rate, the overall ablation on ~~a~~glaciers extensively covered in debris ~~can still exhibit a relatively~~is still significant
80 magnitude (Kääb et al., 2012). These findings imply that understanding of the process and feedback mechanisms
81 governing ablation of debris-covered glaciers in this region is still incomplete. Therefore, it is important to quantify
82 not only the amplitude of melt under time-variable debris cover but also its role in the “Karakoram Anomaly” by
83 assessing the thermal properties of debris layers of different thickness.

84 Field glaciological and meteorological observations on glaciers in the Karakoram are limited by logistical and
85 political constraints (Mayer et al., 2014; Mihalcea et al., 2008). Consequently, a significant knowledge gap exists
86 for debris thickness and its thermal properties as well as the complex coupling of meteorology with heat exchange
87 over glaciers and in debris layers. A limited number of previous melt process investigations under debris layers,
88 e.g., Juen et al. (2014), Evatt et al. (2015), Muhammad et al. (2020), supported by remote sensing observations and
89 climate reanalysis data, have enabled physically-based numerical modeling to provide insight into thermal dynamics
90 within supraglacial debris. For example, Huo et al. (2021b) provided new insights into the relationships between

91 ablation dynamics, surface morphology and debris transport, while Collier et al. (2015) developed understanding of
92 how debris cover affects the atmosphere–glacier feedback processes during the melt season. However, despite these
93 advancements, certain aspects remain insufficiently addressed. Specifically, the seasonal variations and long-term
94 changes in melt patterns, along with the manner in which debris cover exerts its influence on such variations, have
95 not been comprehensively studied. Understanding these dynamics is essential not only for establishing the physical
96 basis of the “Karakoram Anomaly” but also for quantifying the extent to which debris cover contributes to this
97 phenomenon. In this study, we applied an energy-mass balance model ~~coupling~~ coupled with heat conduction within
98 debris layers on Batura Glacier in Hunza valley, Karakoram to demonstrate the influence of debris cover on glacial
99 melt. We aim to: (1) reconstruct the long-term mass balance history of the Batura Glacier, a representative debris-
100 covered glacier in the region; and (2) numerically estimate the distributed ice melt rate under the spatially-
101 heterogeneous supraglacial debris of the Batura Glacier. By enhancing our understanding of glacier mass balance
102 behavior and its relationship to debris cover energy budgets in the Karakoram over the last two decades, this research
103 adds significantly to existing knowledge in this field.

104

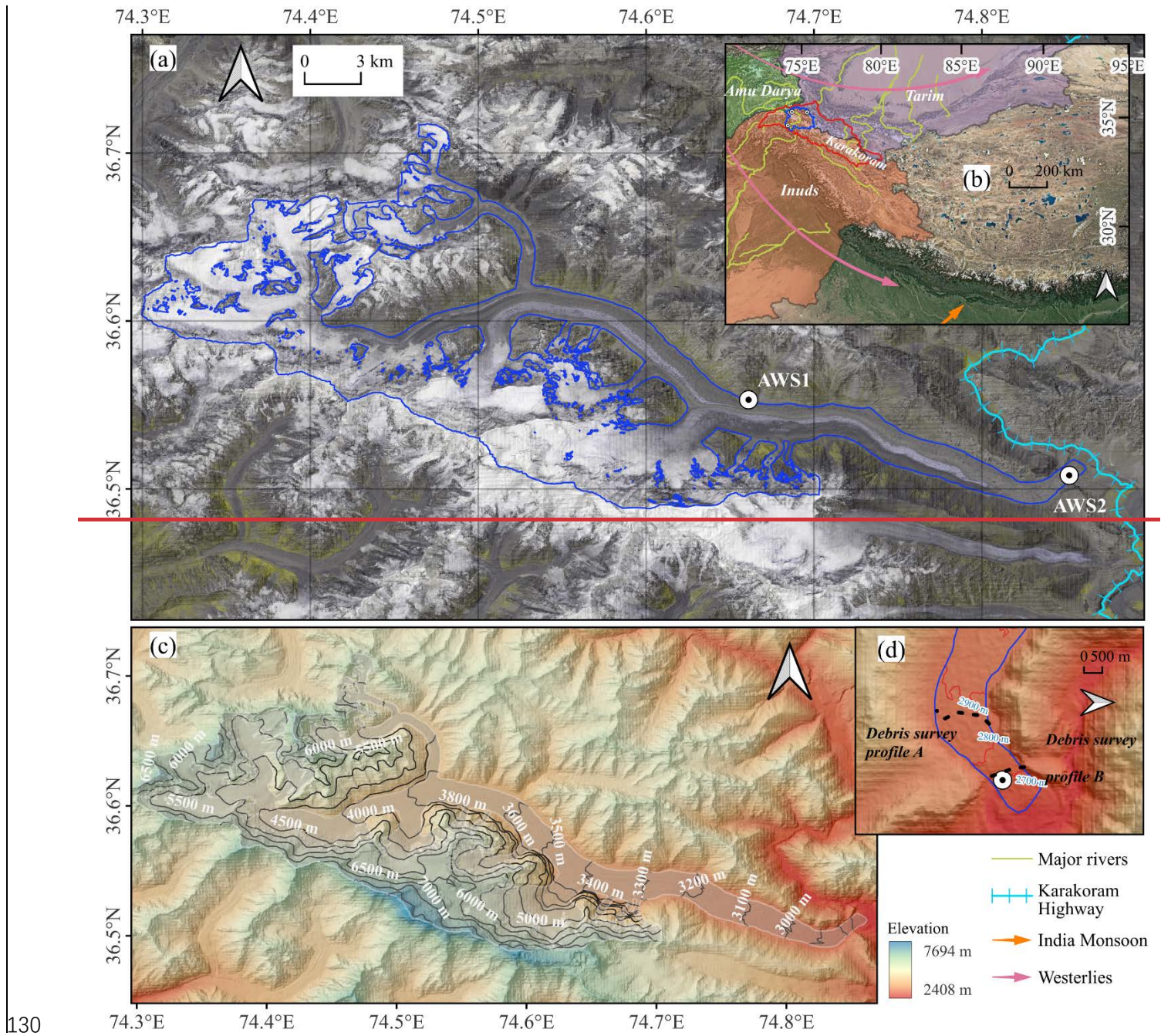
105 2 Study site

106 The Batura Glacier, located in northwest Karakoram, stands as one of the most prodigious valley-type glaciers
107 in the lower latitudes, extending over a length of more than 50 km and encompassing an expansive area exceeding
108 310 km² (Xie et al., 2023) (Figure 1). Approximately 24% (~76 km²) of the glacier's area is covered with debris
109 (Xie et al., 2023), while its thickness in the part below 3000 m a.s.l. surpasses 50 cm (Gao et al., 2020). Due to the
110 heavy debris cover, Batura Glacier presents a hummocky topography and a concave longitudinal surface profile.
111 Because of the large difference in density between ice and debris, the heavily debris-covered glacier section has
112 higher hydrostatic pressure at the glacier bottom (Gao et al., 2020). Influenced by the prevailing Westerlies, the
113 Batura Glacier receives abundant snowfall (exceeding 1000 mm w.e. at altitudes above 5000 meters) in the high-
114 altitude region (Lanzhou Institute of Glaciology and Geocryology, 1980). In addition, the interaction of the South
115 Asian monsoon and Karakoram vortex ~~make-anomalouscause localised~~ cooling over Karakoram, leading to a low
116 air temperature in summer (Dimri, 2021; Forsythe et al., 2017). As observed by (Lanzhou Institute of Glaciology
117 and Geocryology, 1980), the Batura glacier is characterized by a relatively lower average annual air temperature
118 compared to observed glaciers in Tianshan and Himalayas, particularly near the annual snowline, where frigid
119 temperatures close to, or below, 0 °C endure throughout the year, averaging approximately -5°C annually. The

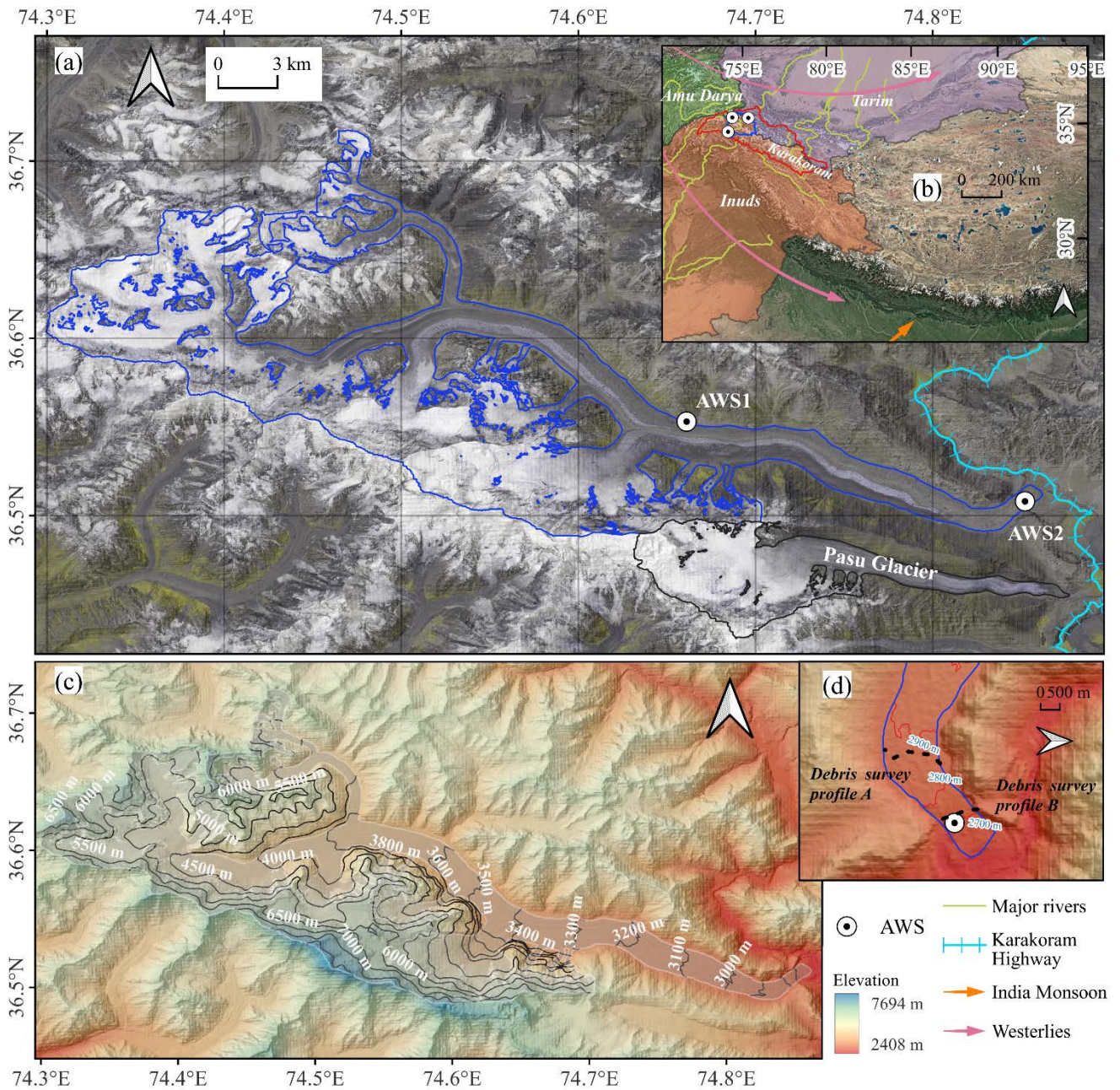
120 glacier displays a rapid flow velocity, with a maximum rate reaching up to 517.5 m yr⁻¹, facilitated by a high rate of
121 mass turnover, and undergoes frequent periods of advance and retreat, while remaining devoid of any surging events
122 (Bhambri et al., 2017).

123 Since the comprehensive investigation on Batura Glacier conducted by Lanzhou Institute of Glaciology and
124 Geocryology during 1974-1975, there has been a scarcity of systematic observations and studies on this glacier.
125 Contemporary investigations of Batura Glacier primarily utilize remote sensing observations, focusing on the
126 glacier dynamics and long-term mass balance, e.g. Rankl and Braun (2016), Wu et al. (2021). There is a challenge
127 in understanding glacier ablation, associated secondary hazards such as glacier floods, and the contribution of
128 glacier runoff to river replenishment.

129



130



131
 132 **Figure 1** Study area. (a) Image of Batura Glacier in 2019 (Synthesized using Sentinel-2 data). (b) Geographic
 133 location of Batura Glacier, with the red line marking-outlining the Karakoram, and the blue line indicating-
 134 outlining the Hunza valley within which, and Batura Glacier is situated within the Hunza valley. The three
 135 weather stations labeled are Khunjerab, Ziarat, and Naltar. (c) Surface Topographyical conditions of Batura
 136 Glacier. (d) Measurement profiles of debris thickness.

137 3 Data and methods

138 3.1 Data

139 3.1.1 Observations

140 An automatic weather station (AWS 1, 74.661° E, 36.550° N, 3390 m) was set up at Batura Glacier on 23

141 September 2013 by the Northwest Institute of Eco-Environment and Resources, Chinese Academy of Sciences
142 (Figure 1a) and has been in continuous operation since then. ~~The location of which is shown in~~ (Figure 1a). Climatic
143 ~~Meteorological variables~~ factors observed at the station are maximum/minimum wind speed and direction,
144 maximum/minimum air temperature, relative humidity, atmospheric pressure, upward and downward long- and
145 shortwave radiations and precipitation, recorded on a daily basis. In this study, we use data from AWS1 in the period
146 23 September 2013 to 9 May 2018 for the bias correction of HAR v2 (High Asia Refined) reanalysis data (Wang et
147 al., 2020) (see section 3.1.2) and for the accuracy assessment of the energy and mass balance simulations. The
148 second AWS (AWS 2, 74.851° E, 36.506° N, 2664 m) was set up in August 2019 by Yunnan University on a debris-
149 covered part of the tongue of the Batura Glacier. The AWS2 records the same climatic factors as AWS1, but it doesn't
150 measure precipitation. We use data from AWS 2 between 1 September 2019 to 25 November 2020 to evaluate the
151 reliability of parameters for energy balance in the debris-covered area. The technical specifications for the sensors
152 used in both AWSs are detailed in Table S1. We additionally used daily maximum/minimum temperatures and
153 precipitation from stations at Khunjerab, Ziarat, and Naltar in the Hunza Valley (Figure 1b) covering the period
154 from January 1, 1999 to December 31, 2008, provided by Water and Power Development Authority (WAPDA),
155 Pakistan, to assess the accuracy of HAR in the Hunza basin.

156 The debris thickness at the terminus of the Batura Glacier (2014) was surveyed by WAPDA and provided by a
157 research group of COMSATS University Islamabad of Pakistan. Additionally, we collected measurements of
158 debris thickness at six sample points near AWS 2 during fieldwork in 2019.

159

160 3.1.2 Reanalysis data

161 The HAR reanalysis data is a product derived from the dynamical downscaling process using the Weather
162 Research and Forecasting (WRF) model. The driving data for the first version is FNL (Final) Operational Global
163 Analysis data, while the second version uses ERA5-atmospheric (0.25°) data (Wang et al., 2020). Compared to
164 the first version, the second version expanded the spatial range of the simulation and extended the time range and
165 will continue to receive updates (see Wang et al. (2020)). In the production of the meteorological variables, the
166 dynamic assimilation of downscaled results was achieved using satellite products and ground observations such as
167 wind speed, wind direction, temperature, and geopotential height. This process significantly improved the accuracy
168 and credibility of the downscaling simulation. Notably, the HAR product has shown great potential in reflecting
169 regional water vapor transport processes (Curio et al., 2015) as well as spatial heterogeneity and seasonal variations

170 in precipitation and temperature (Maussion et al., 2014).

171 3.1.3 Other data

172 The geodetic mass balances for Batura Glacier generated by Brun et al. (2017), Wu et al. (2020), Shean et al.
173 (2020), and Hugonnet et al. (2021) were utilized to validate the energy and mass balance simulation results. These
174 mass balance data were derived from elevation differences with some assumptions such as ice density, etc. ~~Except~~
175 ~~With the exception of the~~for five-year mass balance (2000-2020) produced by Hugonnet et al. (2021), the other data
176 only show the long-term mass balance status after 2000. Time ranges for all mass balance data can be found in
177 Figure- S23. The 30 m resolution DEM ~~with a resolution of 30 meters~~ from the Shuttle Radar Topography Mission
178 (SRTM) was used to generate required terrain factors, while the glacier boundary was defined using the most recent
179 result delineation published by Xie et al. (2023).

180 3.2 Methods

181 3.2.1 The physically-based energy-mass balance (EMB) model

182 The EMB model for snow and ice is a distributed model that combines surface energy processes with a
183 subsurface evolution scheme ~~for~~ snow and ice (COSIPY v1.3) which was developed by Sauter et al. (2020).
184 Details of the model relating to applied parametrizations, physical principles and technical infrastructure have been
185 described in Huintjes et al. (2015b), Sauter et al. (2020) and (Arndt and Schneider, 2023). In common with previous
186 energy balance models, the surface energy budget is defined as the sum of the net radiation, turbulent heat fluxes
187 (including sensible heat flux q_{sh} and latent heat flux q_{lh}), conductive heat flux (q_g), sensible heat flux of rain (q_{rr})
188 and melt energy (q_{me}) (Eq.1). The net radiation is the sum of the net shortwave radiation calculated from incoming
189 shortwave radiation ($q_{sw_{in}}$) and surface albedo (α), incoming longwave radiation ($q_{lw_{in}}$) and outgoing longwave
190 radiation ($q_{lw_{out}}$). To link the surface energy balance to subsurface thermal conduction, the snow/ice surface
191 temperature ($T_{s,si}$) is defined as an upper Neumann boundary condition. The penetrating scheme of shortwave
192 radiation is based on Bintanja and Van (1995).

$$193 \quad q_{me} = q_{sw_{in}}(1 - \alpha) + q_{lw_{in}} + q_{lw_{out}} + q_{sh} + q_{lh} + q_{rr} + q_g \quad (1)$$

194 The glacier melt is solved using q_{me} and penetrating shortwave radiation, while the sublimation is solved
195 using q_{lh} . Combined with the snowfall and refreezing of meltwater (or rain), the total mass balance of the glacier
196 surface can be calculated (Eq.2). The sum of subsurface melt (m_{sub}) ~~triggered by~~ due to penetrating shortwave
197 radiation energy and the refreezing of meltwater (or rain) (refreeze), is defined as the internal mass balance. The
198 internal ablation occurs when temperature at a specific layer reaches the melting temperature (T_m). Internal

199 meltwater, in combination with infiltrated surface meltwater, can be stored in the snow layers. Once a layer [gets](#)
 200 [becomes](#) saturated, meltwater will drain into the next layer until the liquid water content within all layers is less
 201 than a defined ratio, or [else](#) the meltwater runs off when it reaches the lowest model layer. In this process, a part of
 202 [the](#) meltwater refreezes when [the](#) temperature at a layer is less than T_m . [Full D](#)etails for resolving mass and energy
 203 budgets [in the EMB](#) can be found in Sauter et al. (2020).

$$204 \quad mb = \left(\frac{q_{me}}{L_m} + \frac{q_{lh}}{L_v} + \text{snowfall} \right) + (m_{sub} + \text{refreeze}) \quad (2)$$

205 where L_m is the latent heat of ice melt and L_v is the latent heat of sublimation or condensation.

206 The debris energy balance is calculated according to the model of Reid and Brock (2010), and the reader is
 207 referred to their paper for a detailed description of the model. The sum of energy fluxes at the surface is essentially
 208 the same as Eq. 1, but because debris does not melt, the debris surface temperature ($T_{s,d}$) is assumed to change such
 209 that these fluxes sum to zero:

$$210 \quad q_{swin}(1 - \alpha) + q_{lw_{in}}(T_{s,d}) + q_{lw_{out}}(T_{s,d}) + q_{sh}(T_{s,d}) + q_{lh}(T_{s,d}) + q_{rr}(T_{s,d}) + q_g(T_{s,d}) = 0 \quad (3)$$

211 The circularity in solving for $T_{s,d}$ is resolved using a numerical Newton-Raphson method (Eq. 4). Conduction
 212 through the debris is then calculated using a Crank-Nicholson scheme with intermediate temperature layers for a
 213 set depth, and boundary conditions determined by the newly calculated $T_{s,d}$ and the temperature at the debris-ice
 214 interface, which is assumed to stay at zero (Eq. 5). The ablation rate is determined from the conductive heat flux to
 215 the first [uppermost](#) ice layer, found using the temperature gradient between the lowest debris layer and the ice (Eq.
 216 6). The detailed solution processes for Eq. 4-6 can be found in Figure 2 and Appendix materials in Reid and Brock
 217 (2010).

$$218 \quad T_{s,d}(n+1) = T_{s,d}(n) - \frac{fun(T_s(n))}{fun'(T_s(n))} \quad (4)$$

219 where, $T_{s,d}(n)$ and $fun(T_{s,d}(n))$ refer to the temperature and the total energy flux at nth debris layer. The
 220 termination condition for this solution is set as $T_s(n+1) - T_s(n) < 0.01$.

$$221 \quad q_G = -k_d \left(\frac{dT_s}{dz} \right) \approx k_d \frac{T_{s,d}(N-1) - T_m}{h} \quad (5)$$

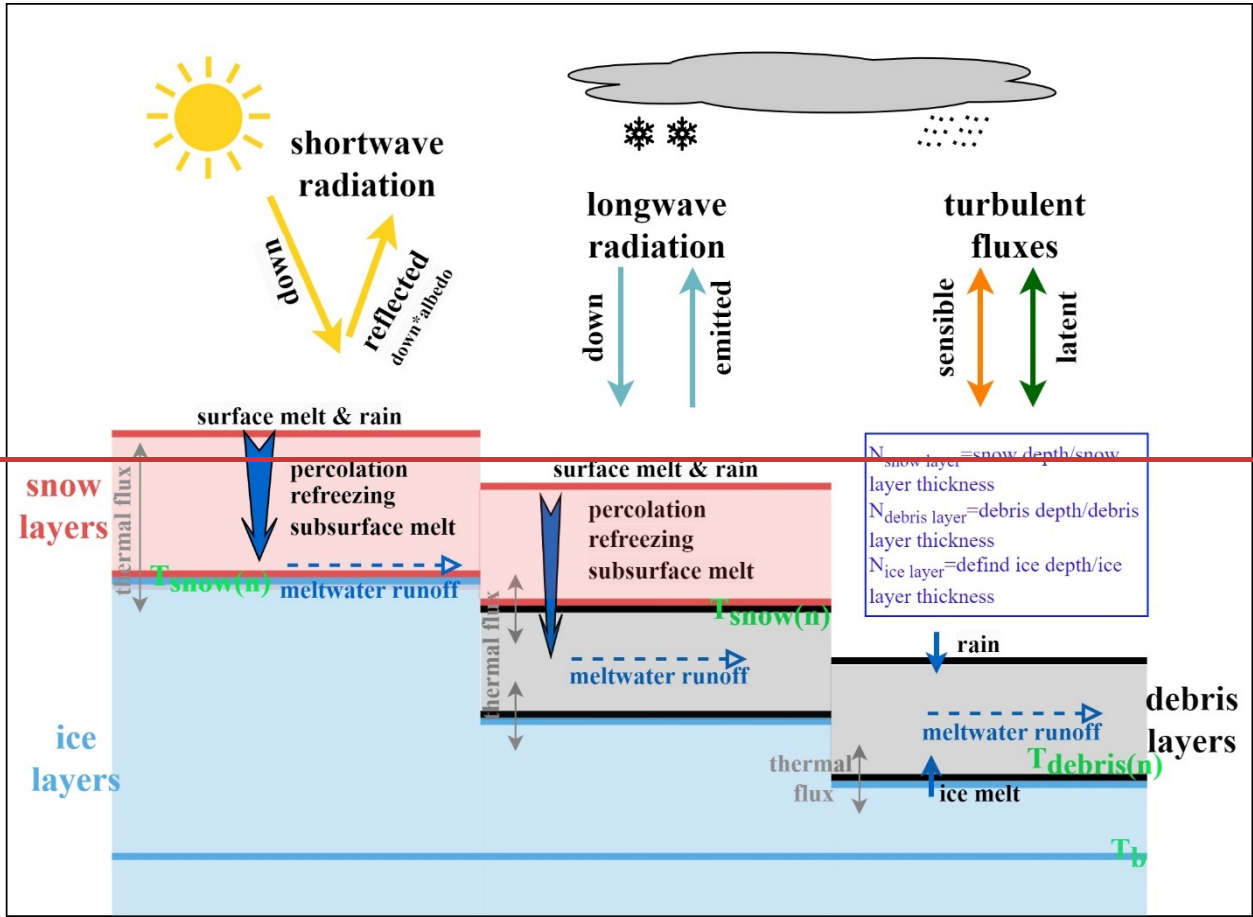
$$222 \quad Melt_{deb} = \frac{q_G}{\rho_i L_f} \quad (6)$$

223 where, h represents the thickness of each layer, n represents nth debris layer, N represents the number of
 224 calculation layers, T_m represents the melting temperature of ice, and k_d is the thermal conductivity of
 225 supraglacial debris. $Melt_{deb}$ refers to [the](#) ablation [rate of ice at the](#) [under](#) debris [interface](#).

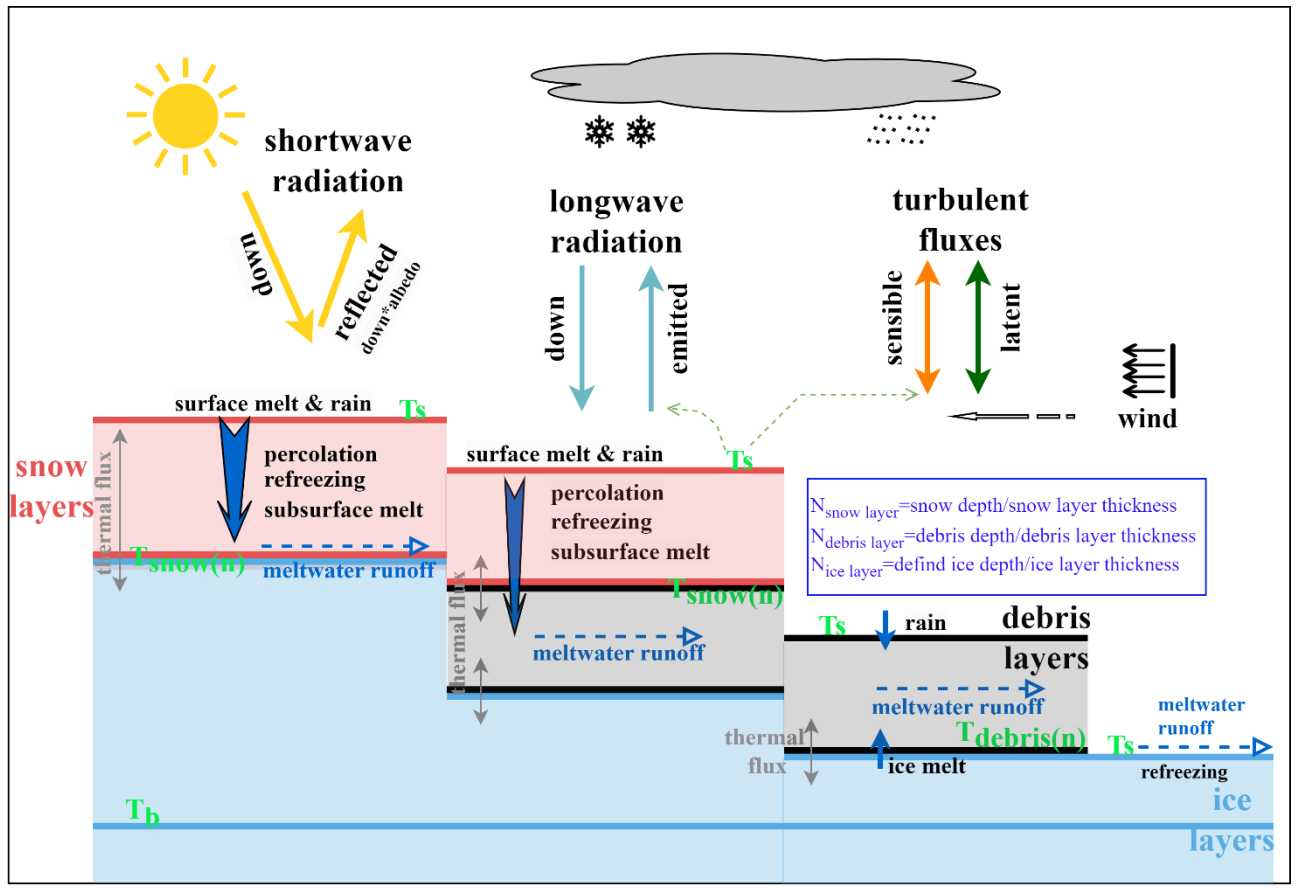
226 In the model run, the initialization of the model was firstly conducted using the defined parameters. The most

227 important in this step was the ~~initialization-establishment~~ of the temperature profile, which was initialized with air
228 temperature (T_a) and bottom temperature (T_b) by using linear interpolation. The second step involved~~s~~ recalculating
229 the temperature profile, involving two scenarios: (1) In debris-free area~~s~~, the temperature profile was calculated
230 entirely according to the COSIPY. Initially, the temperature profile was computed without considering the impacts
231 of refreezing or subsurface melt~~s~~, but factoring in temperature increase due to penetrating radiation~~-only~~. If a
232 snow/firn pack is present, the densification of the dry snow pack was calculated using an empirical relation (Herron
233 and Langway, 1980). After densification, the available surface and subsurface meltwater percolated downward, with
234 a small amount retained in each layer. Subsequently, the temperature changes resulting from refreezing of meltwater
235 were computed, updating the subsurface layer temperature. In debris-covered areas, when snow presented, the snow-
236 debris interface temperature was first obtained using ~~the~~ snow layer temperature update scheme of the COSIPY
237 model. This temperature was ~~then~~ set as the ~~debris~~ surface temperature~~-of the debris then~~. By defining the debris-
238 ice interface temperature as zero, the debris layer temperature was then calculated using Eq. 5. In the absence of
239 snow, the model employs the debris layer temperature update scheme described by Reid and Brock (2010). The
240 third step involved~~s~~ using the surface temperature obtained from the second step, combined with glacier surface
241 meteorological parameters, to calculate the surface energy balance and surface melt. The primary physical processes
242 of the model are illustrated in Figure 2. In this study, a two-year spin-up was implemented to allow the model to
243 adapt to the surrounding conditions (Huintjes et al., 2015a).

244



245



246 **Figure 2** General scheme of the model used in the current study with fluxes and physical processes. T_s represents
247 surface temperature, solved for using the heat conduction equation. The solution process varies depending on the
248 different surface cover conditions of the glacier. T_s is a crucial variable linking the energy exchange between
249 the glacier and the atmosphere. T_s is primarily used to calculate sensible heat flux and emitted longwave
250 radiation. Reflected shortwave radiation is mainly determined by surface albedo. In the case of snow cover, the
251 albedo changes continuously with snowmelt and densification. $T_{snow(n)}$ represents the temperature of the nth snow
252 layer, reflecting the energy flux at the snow-ice interface or snow-debris interface. $T_{debris(n)}$ represents the
253 temperature of the nth debris layer, reflecting the energy flux at the debris-ice interface. These two variables are
254 important for characterizing the internal energy balance of the glacier.

255 In the model, the layers of snow, debris, and ice were dynamically calculated based on their individually
256 specified thicknesses. Considering that the temperature of the ice layer does not change with increasing thickness
257 below a certain depth in glaciers, a depth of 10 m for the ice layer was set, following Huintjes (2014). As ice
258 temperature cannot exceed 0 °C, the boundary conditions at snow-debris interfaces were configured similarly,
259 following an analogous scenario that the temperature of snow-debris interface remains below 0 °C (Giese et al.,
260 2020). Based on this, we made the assumption that any rain or snowmelt water does not refreeze within the debris
261 layer, and the infiltration of such water does not alter the temperature of the debris layer. The temperature boundary
262 condition at the debris-ice interface follows Reid and Brock (2010), ensuring that the temperature of debris-ice
263 interfaces remains below 0 °C. For the lower boundary condition (bottom temperature), values referenced from
264 Huintjes (2014) are employed, derived from observational data. To prevent ice layer temperatures from surpassing
265 exceeding freezing level, a heating mechanism is applied to the ice layer above the bottom layer, concentrating
266 directing above-freezing energy into the melting process.

267 In this study, the model simulations were conducted by using a high-performance server, equipped with dual
268 Intel Xeon CPU E5-2687W processors (48 threads), 768 GB of RAM, and dual Quadro P6000 (24G) GPUs for
269 acceleration. We conducted simulations that compared scenarios with and without supraglacial debris on the Batura
270 Glacier to assess the influence of debris on mass balance.

271 3.2.2 Model setup and input data

272 In this study, HAR v2 data were used to drive the model to simulate the energy and mass balance of the Batura
273 Glacier from 2000 to 2020. The meteorological variables in HAR v2 selected to meet the requirements of the energy
274 balance simulation include precipitation, air temperature at 2 m, wind speed (u - and v - components at 10 m),

275 atmospheric pressure, specific humidity, downward shortwave radiation, and cloud cover. The 10 m wind speed was
276 converted to 2 m using an empirical formula provided by Allen et al. (1998), while specific humidity was converted
277 to relative humidity using the formula given by Bolton (1980) utilizing the 2 m air temperature and atmospheric
278 pressure. Air temperature was calibrated at the basin scale using a gridded bias factor. The gridded bias was
279 interpolated by the nearest-neighbor method, with the bias at each station calculated between [the](#) observed and HAR
280 temperatures. After correction, a small bias range of $\pm 1^\circ\text{C}$ was observed between HAR temperature and station
281 temperature, with a Pearson correlation coefficient of 0.98. Details regarding [the](#) precipitation calibration can be
282 found in Appendix A1. Due to lack of observations for other variables, no further validation before statistical
283 downscaling was conducted at the basin scale in this study. However, minor adjustments were applied for
284 downscaled other variables. These adjustments were made using scale factors calculated through the least squares
285 method, considering the downscaled results and observed values at the two stations on Batura glacier.

286 We utilized the data from Rounce et al. (2021) based on an inversed energy balance modeling procedure [as-to](#)
287 [calculate](#) debris thickness inputs. [The debris thickness with a 100 m resolution is resampled to 300 m using an](#)
288 [inverse distance weighted interpolation method to match the simulation resolution.](#)— We validated the simulated
289 debris thickness using observed data, which showed an average deviation of 6 cm. However, it should be noted that
290 the Rounce et al. (2021) results significantly underestimated the debris thickness at certain locations near the
291 terminus of the glacier. For instance, at AWS2, the observed debris thickness was approximately 1.13 m, whereas
292 the inverted thickness was only 0.47 m.

293 The simulation was conducted at a spatial resolution of 300m and a temporal step of 1 day. The primary
294 meteorological drivers, such as precipitation and temperature, were calibrated using data from meteorological
295 stations. We employed statistical methods to downscale all meteorological inputs to a resolution of 300 m (for more
296 details, please refer to the supplementary [methodsmaterial](#)). The simulation grid was constrained using the glacier
297 boundaries from Xie et al. (2023), and no ice flow dynamic adjustments for the glacier were considered. In this
298 study, we also conducted a simulation on the debris-free Pasu Glacier situated adjacent to the Batura Glacier to
299 make [a](#) comparative study of [fr](#) mass and energy balance. We assumed that Pasu Glacier experiences similar climatic
300 conditions to Batura Glacier. The physical parameters used for this simulation are identical to those from AWS1 on
301 Batura Glacier (see the Section 3.2.2) and we compared the simulated mass balance with the geodetic mass balance
302 to test the extension of these parameters.

303

304 3.2.3 Parameters calibration/ validation

305 In this study, we used ~~the~~ value ranges for most parameters which have been acquired from empirical equations,
306 large extent observations, ~~and-or~~ physical processes simulations in previous studies e.g., Reid and Brock (2010),
307 Mölg et al. (2012), Hoffman et al. (2016), Zhu et al. (2020), and Sauter et al. (2020). Since the model is ~~much-very~~
308 complex, ~~it was necessary to~~ ~~we must~~ constrain the number of calibrated parameters to limit the modeling effort.
309 Through sensitivity analysis at AWS1, we identified four parameters that have significant impacts on simulating
310 mass balance; ~~including~~ ice albedo and roughness length of ice, which constrain ice melting ~~addressing both~~ ~~through~~
311 the radiative and turbulent energy fluxes, ~~respectively~~; and firn albedo and roughness length of firn, which control
312 the snow evolution processes. By adjusting these parameters ~~within a~~ specific step range, our goal was to achieve
313 the closest match between simulated albedo ~~and~~, longwave radiation ~~and~~, ~~with~~ their observed values ~~by~~ using a self-
314 defined $RMSE_{score}$. The $RMSE_{score}$ is calculated as Eq.7.

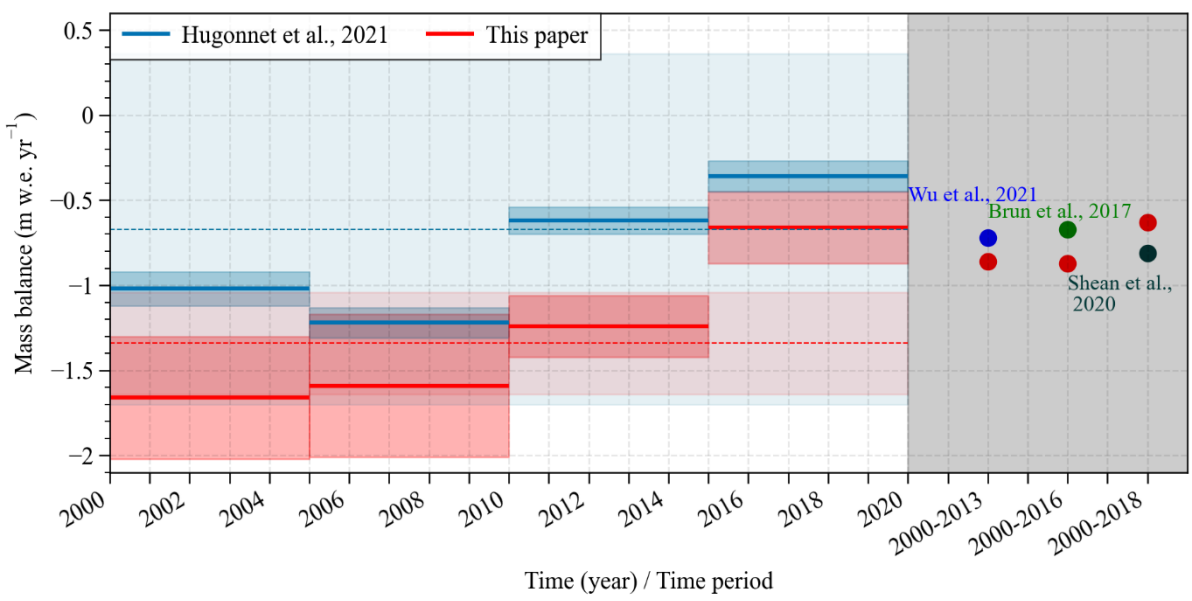
$$315 \quad RMSE_{score} = \sum_{k=1}^n \sqrt{\frac{1}{m} \sum_{i=1}^m (obs_std_{k,i} - sim_std_{k,i})^2} \quad (7)$$

316 Where n represents the number of variables, obs_std_k and sim_std_k represent the standardized observed and
317 simulated values of k th variable. The standardization is achieved through ~~m~~Min-~~m~~Max ~~n~~Normalization. For the
318 purpose of comparison, the final $RMSE_{score}$ is presented as a standardized result ranging from 0 to 1. A smaller
319 $RMSE_{score}$ indicates better performance of the model. By comparing the $RMSE_{score}$, we can easily determine the
320 optimal values for calibrating the parameters (Figure S1). The final determined values for the selected parameters
321 are show in Table S2. With these parameters, the RMSE between simulations and observations on albedo and
322 outgoing longwave radiation are 0.09 and 18.93 W/m², respectively, and there is a high degree of correlation
323 between observations and simulations on annual variations, with Pearson correlation coefficients (~~eer~~) of 0.83 for
324 albedo and 0.86 for outgoing longwave radiation (Figure S2). After determining the primary parameters, we fine-
325 tuned some independent parameters such as albedo timescale, albedo depth scale, temperature threshold of
326 rain/snow ratio, ensuring a comparable level of simulated mass balance with geodetic mass balance. The simulated
327 mass balance agrees well with the geodetic mass balance, with an average bias of 0.27 m w.e.: ~~ParticularlyIn~~
328 ~~particular~~, there is a strong agreement between the results from Hugonnet et al. (2021) and our simulations in terms
329 of the trend observed from 2000 to 2020 (Figure 23). This indicates that the parameters used in our study can reliably
330 estimate the mass and energy budget.

331 A point simulation at AWS2 was conducted to calibrate and validate the parameters required to simulate energy
332 balance in debris layers. Following Giese et al. (2020), we ~~ascertained~~ ~~evaluated~~ the ~~model~~ parameters by ~~evaluating~~

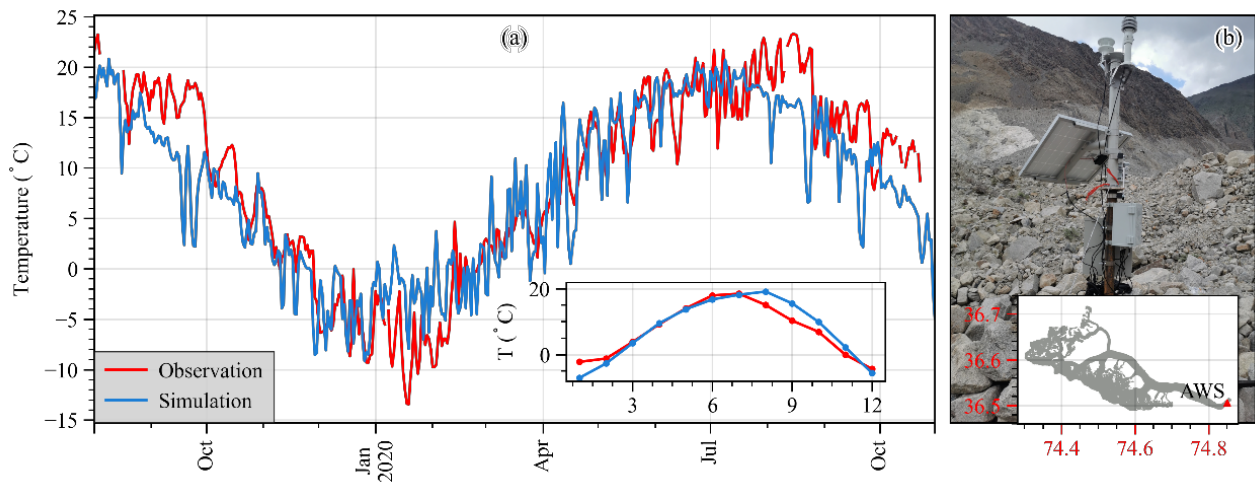
333 [optimizing](#) the agreement between the simulated surface temperature and the surface temperature recorded by AWS
 334 2 (The temperature probe is buried ~ 2 centimeters below the [debris surface layer](#)). The parameters calibrated at
 335 AWS1 were ~~entirely~~ applied [unchanged](#) to AWS2, with ~~only~~ adjustments [only](#) made to the debris thermal
 336 conductivity and debris albedo during the simulation process. The calibration process can be observed in Figure S3.
 337 Figure ~~3-4~~ depicts the comparative analysis of the observed station temperature and the simulated temperature, [using](#)
 338 [the optimized values for debris thermal conductivity and albedo](#), revealing a ~~commendable~~ [strong](#) consistency
 339 between the two over time, ~~exhibiting with~~ a correlation coefficient of 0.87. ~~A~~ although there is a tendency to
 340 underestimate the temperature in late summer and autumn, and overestimate temperature in late winter. The
 341 correlation of observed and simulated temperature for the annual cycle is 0.96, while the RMSE during the
 342 simulation period is 0.86 °C.

343 ~~In fact,~~ The parameter ~~calibration-evaluation~~ process at AWS2 ~~involved the extension of the parameters~~
 344 ~~calibrated at AWS1, confirming supports~~ the applicability and scalability of ~~these the~~ parameters [calibrated at AWS1](#)
 345 [to other parts of the glacier](#). ~~This is because the calibration of these two parameters at AWS2 is independent of other~~
 346 ~~previously calibrated parameters. Additionally,~~ Based on the final parameters determined (Tables S2 and S3), the
 347 simulated mass balance for the entire glacier is estimated to be -0.23 m w.e. yr⁻¹ (2000-2016). ~~This value~~ closely
 348 aligns with the geodetic mass balances derived from remote sensing (-0.18 m w.e. yr⁻¹, spanning the years 2000-
 349 2016, Brun et al. (2017); -0.39 m w.e. yr⁻¹, covering the years 2000-2009, Bolch et al. (2017); and -0.24 m w.e. yr⁻¹,
 350 covering the years 2000-2014, Wu et al. (2020)). This further ~~corroborates~~ [supports](#) the ~~rationality~~ [robustness](#) of
 351 parameter ~~extension~~ [transfer across the glacier](#). ~~The final parameters can be found in Table S2 and S3.~~



352

353 **Figure 2-3** Comparison of simulated and geodetic mass balance over different time periods. To assess the
 354 performance of our model, we compared the simulated mass balance with estimates derived from geodetic
 355 observations. However, it is important to acknowledge that this approach introduces a degree of dependence
 356 between the two results since some model parameters were calibrated using the geodetic mass balance.



358 **Figure 3-4** (a) Observed and simulated surface temperature at AWS 2. (b) Photograph and location of AWS 2 on
 359 Batura Glacier. AWS 2 collects data at both daily and hourly intervals, this study utilizes daily records for
 360 analysis.

362 4 Results and discussions

364 4.1 Glacier climatic-mass-balance dynamics and corresponding energy budgets

365 4.1.1 Energy budgets

366 During 2000-2021, the surface net radiation of the Batura Glacier accounted for the largest proportion of total
 367 energy heat flux (46%), followed by sensible heat flux (23%). Both latent heat flux (-18%) and conduction
 368 conductive heat flux (17%) demonstrated a similar magnitude of contribution to the total energy heat flux, albeit
 369 with opposite sign-

370 As presented in (Table 1). T, the net shortwave radiation accounted for 85% of the total energy influx (77
 371 W/m²), while sensible heat constituted 15% (14 W/m²). Regarding energy sink components, net longwave radiation
 372 contributed ~~to~~ 57% (52 W/m²), melt heat ~~to~~ 20% (18 W/m²), latent heat ~~to~~ 12% (11 W/m²), and conductive heat ~~to~~
 373 11% (10 W/m²). In terms of the energy components that contribute to glacial mass loss, sublimation latent heat

374 accounted for approximately 38%, while the energy ~~directly responsible~~ for snow/ice melting constituted 62%. For
 375 the Batura Glacier, roughly 32% (29 W/m² out of 91 W/m²) of the surface energy influx was consumed by glacier
 376 mass loss, a proportion similar to that of Muztag Ata No.15 Glacier, which is also situated in the Westerly influenced
 377 area (30%, 26 W/m² out of 89 W/m²) (Zhu et al., 2017). However, it is worth noting that the melting heat of the
 378 Batura Glacier was significantly higher than that of Muztag Ata No.15 Glacier (~2 W/m²), possibly due to disparities
 379 differences in surface debris cover between the two glaciers.

380 During the period of accumulation, a notable proportion of 73% of the energy influx of the Batura Glacier was
 381 expended through net longwave radiation, with 15% of the energy utilized for snow/ice sublimation, leaving the
 382 remaining portion dedicated to thermal conduction within the debris cover or snow layer. In contrast, throughout
 383 the ablation season, the energy influx was mostly from net shortwave radiation, specifically amounting to 133 W/m².
 384 The ~~thermal-conductive heat flux~~ exhibited by the Batura Glacier diverged significantly from debris-free glaciers,
 385 such as the Guliya ice cap (Li et al., 2019). In the Batura Glacier, a considerable portion of the energy influx at
 386 lower elevations was absorbed by the debris cover, resulting in higher surface temperatures compared to the lower
 387 layers, thus yielding heat transfer towards the debris-ice interface. Conversely, in the accumulation area, the primary
 388 source of energy was dedicated to heating the snow layer. It became evident that during the ablation season, the
 389 debris cover assumed a more prominent role, ultimately leading to an overall negative thermal conduction.

390
391
392
393
394
395
396
397

Table 1 The energy budget on Batura Glacier. lw_{in} and lw_{out} denote Incoming and outgoing longwave radiation, sw_{in} and sw_{out} denote Incoming and outgoing shortwave radiation, sh and lh represent the sensible heat flux and latent heat flux, g represents conductive heat flux, and me represents melt energy. All values are expressed in W/m².

Periods	lw_{in}	lw_{out}	sw_{in}	sw_{out}	Net lw	Net sw	Net radiation		sh		lh		g		me
							—	%	—	%	—	%	—	%	
Annual average	212	-264	249	-172	-52	77	25	42	14	23	-11	18	-10	17	18

Ablation (6-9)	231	-293	345	-212	-62	133	71	65	-7	6	-15	14	-16	15	33
Accumulation (10-5)	202	-249	187	-153	-48	34	-12	19	32	52	-10	16	-8	13	0

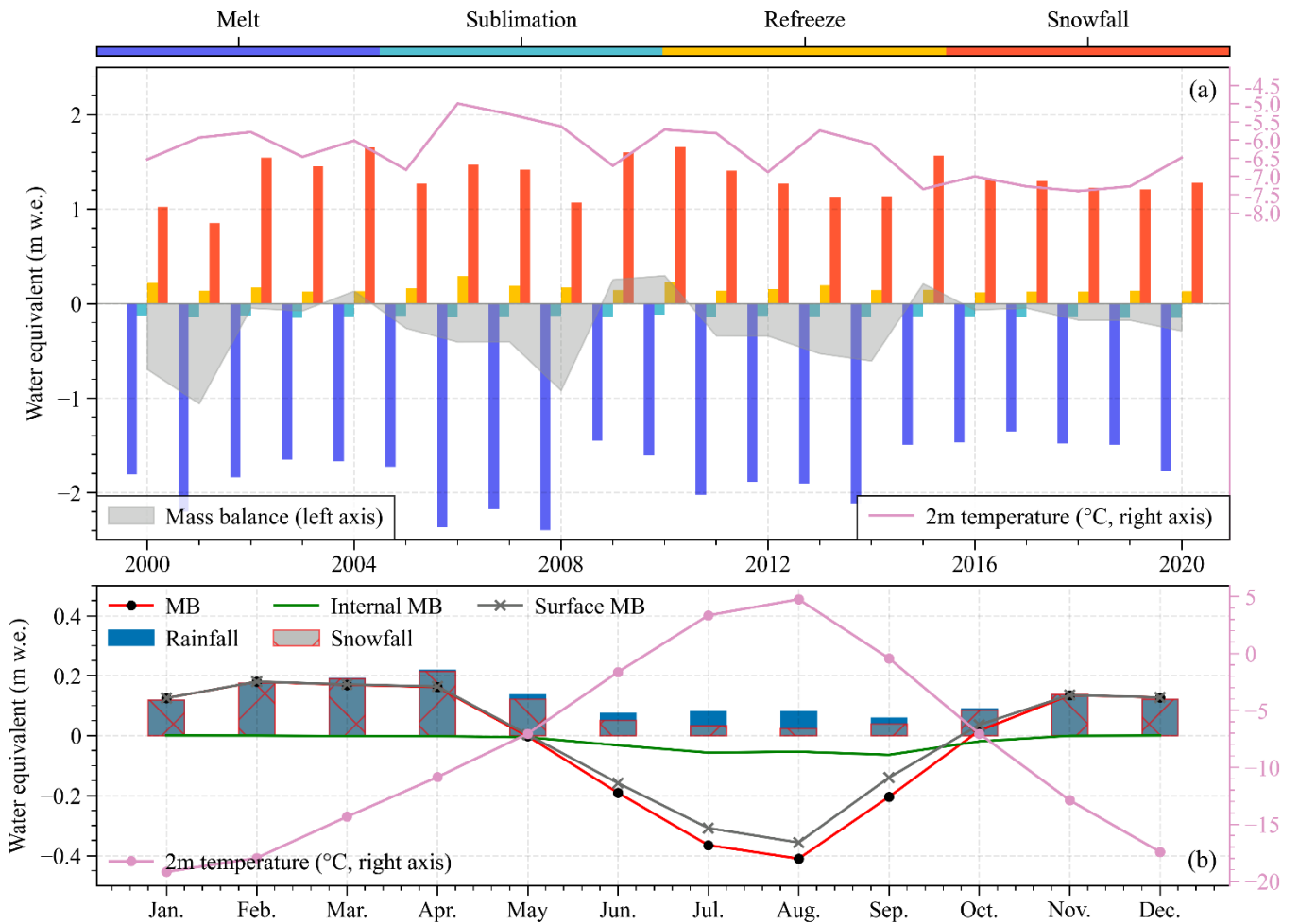
398

399 4.1.2 Mass balance history

400 The results from the [energy balance-EMB](#) model show that the average mass balance of the Batura Glacier
401 during the studied period was -0.262 ± 0.561 m w.e. yr⁻¹ (Table 2). The glacier experienced its highest positive mass
402 balance in 2010 (0.32 m w.e. yr⁻¹) and its greatest negative mass balance in 2001 (-1.19 m w.e. yr⁻¹). Snowfall was
403 the primary source of glacier mass gain, accounting for 89% of the total mass gain. Refreezing mitigated the internal
404 melting caused by radiation penetration and contributed to 11% of the mass accumulation. Glacier melting
405 constituted 92% of the mass loss, while sublimation/evaporation, which exhibited minimal interannual variability,
406 contributed only 8% to the mass loss.

407 The model simulations show a decline in glacier ablation after 2008, accompanied by a decrease in the absolute
408 magnitude of the mass budget over the study period (Figure 4a5a). Independent measurements of thinning rates at
409 the glacier terminus measured by ground-penetrating radar, declined from 4.58 m yr⁻¹ between 1974-2000 to 0.59
410 m yr⁻¹ after 2000 (Gao et al., 2020), implying a similar reducing trend in surface melt rate, which further [strengthens](#)
411 [the consistency with our research supports the EMB](#) results. The [incredible striking decreased difference](#) in the
412 thinning rates at Batura Glacier for the periods 1974-2000 and 2000-2017, [and decline in modeled ablation since](#)
413 [2008](#) might be linked to regional climate fluctuations. Previous studies based on station observations have indicated
414 a notable cooling trend in the upper Indus River basin during the summer months, particularly in July, September,
415 and October, from 1995 to 2012 (Hasson et al., 2017). Moreover, there was a lack of long-term warming during the
416 winter months over the same period (Hasson et al., 2017). Forsythe et al. (2017) suggested that the summer
417 temperature in the Karakoram was relatively low and exhibited a decreasing trend due to the influence of the
418 Karakoram vortex (KV). This influence may have contributed to the notably higher positive accumulated
419 temperatures pattern observed from 1970 to 2000 compared to those recorded after 2000, as shown in Figure 4b of
420 Forsythe et al. (2017). Our analysis on air temperature in the Hunza basin from 1980-2020, utilizing ERA5 data,
421 corroborates these findings (Figure S4).

422 As shown in Figure [4b5b](#), the variations in internal mass balance and surface mass balance are generally
423 consistent throughout the year, both showing a negative mass balance from June to September. During this period,
424 there was a high shortwave radiation and, consequently, a great amount of shortwave radiation penetrated into
425 snow/ice. This increased ablation resulted from penetration radiation, coupled with relatively high temperature,
426 reducing the rate of refreezing, and thus causing a negative internal mass balance. The mass budgets in May and
427 October were transitional between accumulation and ablation periods. The seasonal pattern on mass balance
428 observed in this study is generally similar to that of the Siachen Glacier, [East Karakoram](#) presented by Arndt and
429 Schneider (2023). Both glaciers exhibit a characteristic of winter/spring accumulation. However, the [modeled](#)
430 meltwater during the ablation season ~~is was found to be~~ significantly lower for Siachen Glacier compared to Batura
431 Glacier. It is worth noting that Arndt and Schneider (2023) did not consider the impact of supraglacial debris cover
432 on glacier melt, which is known to be substantial (Agarwal et al., 2016). Even without considering the debris cover,
433 the mass balance of Siachen Glacier, as indicated by Arndt and Schneider (2023), can still remain in equilibrium,
434 largely depending ~~ent~~ on the [precipitation and temperature](#) driving data, ~~particularly precipitation and temperature~~.
435 On the other hand, in the simulation study conducted by Kumar et al. (2020), Siachen Glacier exhibited a negative
436 mass balance during the same period, with the average temperature and precipitation being higher than those used
437 by Arndt and Schneider (2023). This suggests that simulation results can be considerably influenced by model inputs,
438 and this will be discussed in Section 4.5.



439

440

441

442

443

Figure 4-5 Interannual (upper panel) and mean annual-monthly (lower panel) characteristics of the glacier-wide average of mass components on Batura Glacier over the study period. The MB denotes mass balance. The 2m temperature is obtained from the simulated results.

Table 2 Mean values of the mass balance components of Batura glacier over 2000 to 2020.

	Mass balance	Snow accumulation	Surface melt	Refreezing	Sublimation
Values (m w.e. yr ⁻¹)	-0.262±0.561	1.325±0.174	1.613±0.394	0.162±0.125	0.136±0.005
Proportion of mass gain (loss) (%)	—	89	(92)	11	(8)

444

445

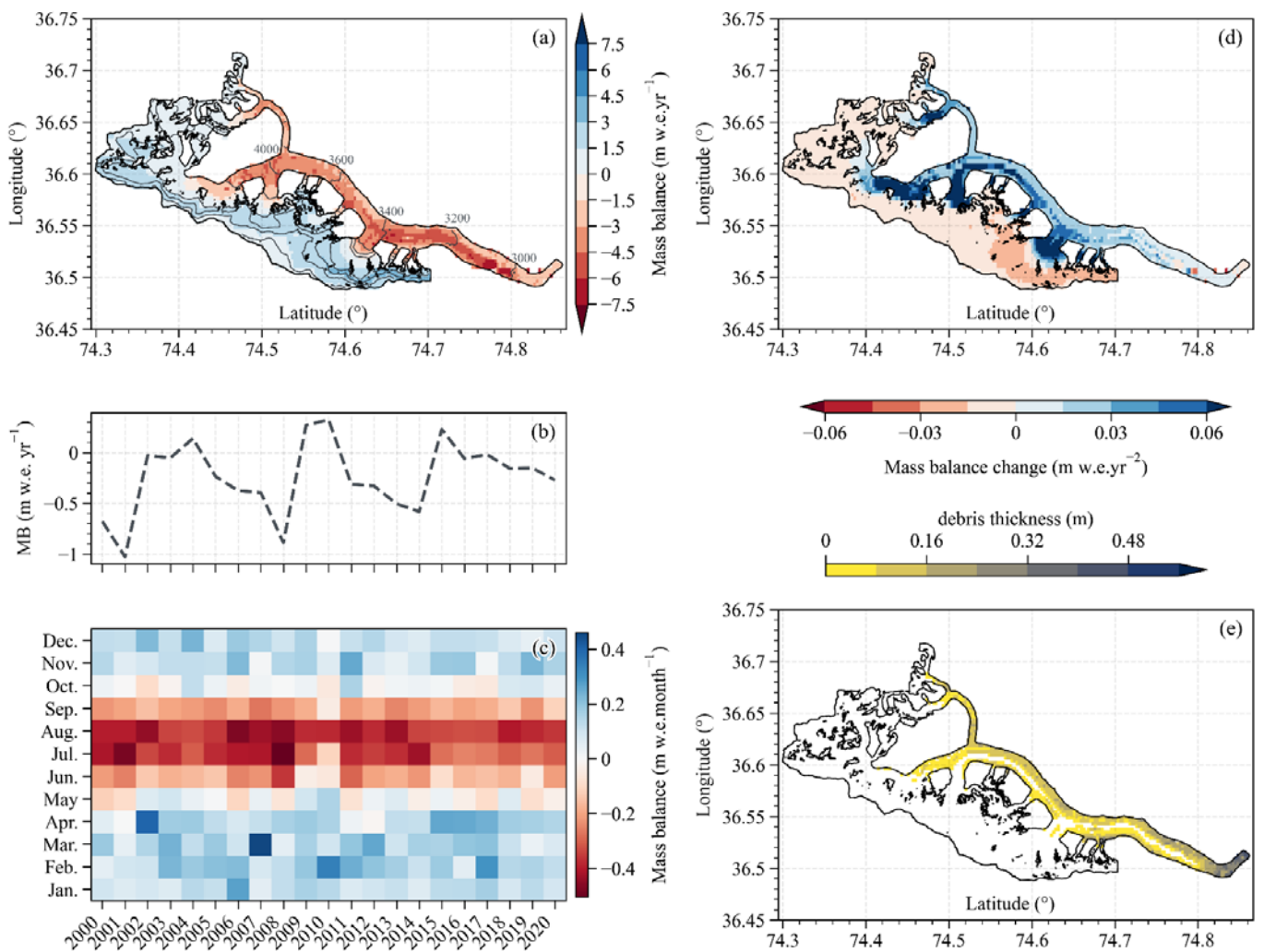
446

Over the study period, the glacier demonstrated a positive rate of annual mass balance change of 0.023 m w.e. yr⁻², indicating the glacier's mass balance was becoming less negative and approaching equilibrium between 2000-

447 2020 (Figure 5a6a, b and d). Particularly noteworthy is the trend of decreasing mass loss across the ablation zone,
448 which is particularly pronounced in the junction where debris cover and bare ice intersect and the tributary where
449 debris cover is thin or absent (Refer to debris cover in Figure 5e6e), which indicates a reduction in melt (Figure
450 5b6b). Given the rate of mass balance change over time (reduction of melt) is highest in these areas, the mass
451 changes in these areas probably have a large impact on the trend of decreasing negative mass balance.

452 Across the entire accumulation zone, a slight decrease in mass gain over the 2000-2020 period was observed,
453 with a more pronounced reduction in mass gain observed on the southern flank of the accumulation area, likely
454 associated to diminished winter snowfall. From a mass budget perspective, the glacier's mass balance appears to be
455 approaching equilibrium, likely due to the reduced melting during the months of June and July (Figure 5e6c). For
456 instance, in years characterized by a positive mass balance, such as 2010, the duration of mass accumulation in
457 spring extended, accompanied by minimal mass loss during June and July. The glacier's mass balance generally
458 followed a cyclic pattern spanning roughly five-seven years. The mass balance has become more negative after
459 2016, possibly indicating a phase of reduced snow accumulation— gain (Figure 5e6c).

460



461
 462 **Figure 5-6** Spatial distribution of the annual mass balance over the 2000-2020 period (a). Time series of modeled
 463 annual (b) and monthly (c) mass balance from 2000-2020. Spatial distribution of the annual mass balance change
 464 rate over the 2000-2020 period (d). Spatial distribution of debris thickness (e)

465 4.2 Energy and mass budgets along the altitudinal profile

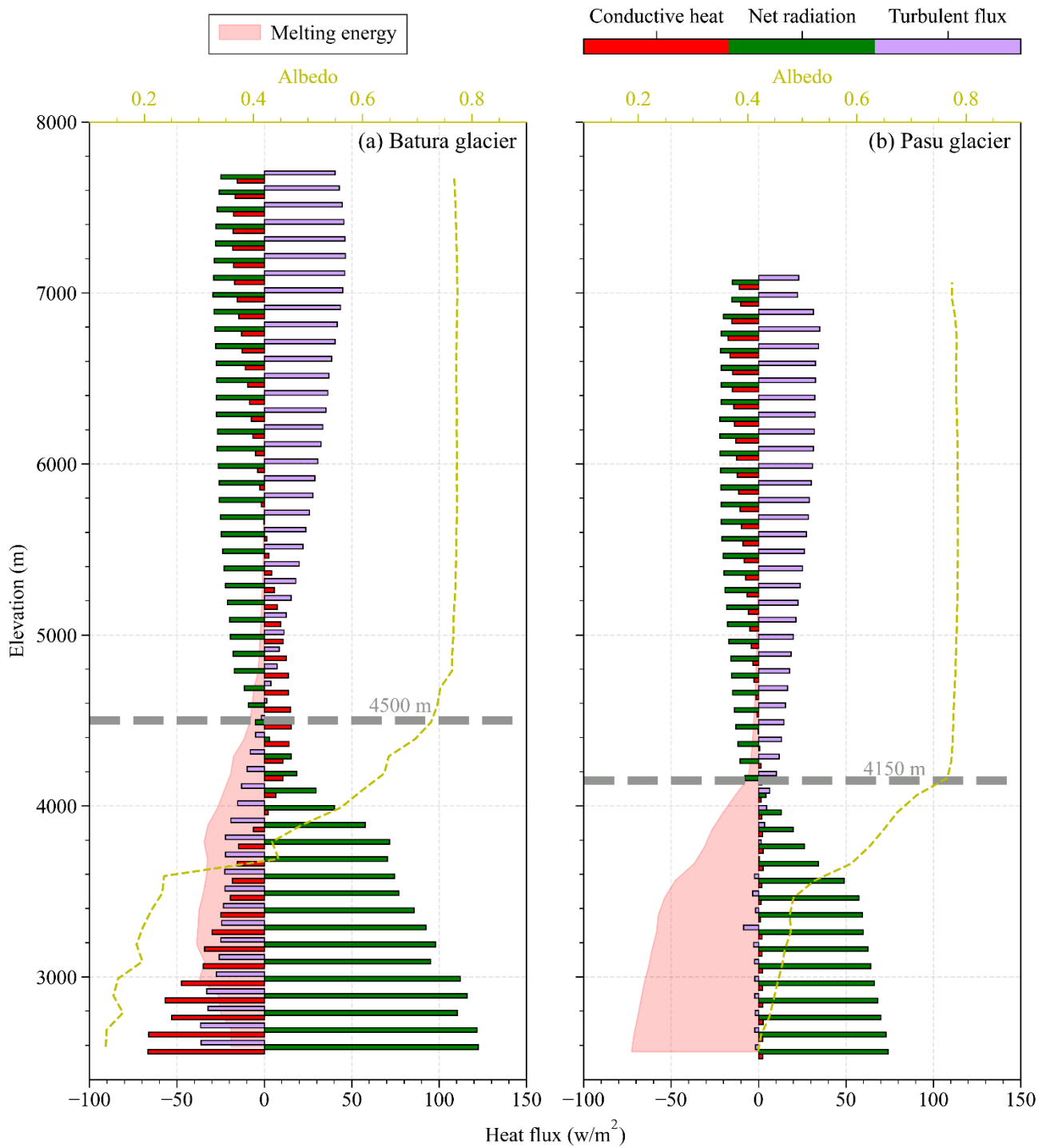
466 A significant heterogeneity of mass balance was observed in the Batura Glacier. The mass gain in the glacier
 467 accumulation zone can reach up to almost 2 m w.e., whereas terminus melting exceeded 4 m w.e. between 3000-
 468 3800 m, with the maximum melting of 4.6 m w.e. occurring within the elevation range of 3350-3450 m. Mass
 469 balance exhibited discernible altitude-dependent distribution, whereby the most substantial melting was observed
 470 not at the terminus but rather in the range between 3000 and 3400 m (Figure S5a).

471 A comparative analysis was performed to understand the variations in mass balance across different elevation
 472 zones between Batura Glacier and Pasu Glacier. The equilibrium line altitude (ELA) of the Batura Glacier (4500 m)

473 was significantly higher than that of the Pasu glacier (4150 m). Below the ELA, both glaciers exhibit gentle overall
474 slopes, leading to high receipt of solar shortwave radiation. As shown in Figure 67, the net radiation of the Batura
475 Glacier was significantly larger than that of the Pasu glacier, primarily attributable to surface albedo disparity. The
476 Pasu Glacier's surface primarily comprises firn or ice, whereas the Batura Glacier is largely covered with fragmented
477 rocks with associated lower albedo. Evidently, the sensible heat of melt energy for the Batura Glacier is less than
478 that of the Pasu Glacier, chiefly due to heat conduction between debris layers, which absorb a substantial amount
479 of energy. Overall, the Batura Glacier demonstrated a "bowarch-shaped" melt energy pattern from its terminus to
480 the ELA, in sharp contrast to the "slope-increasing" pattern exhibited by the Pasu Glacier. This altitude-dependent
481 spatial energy distribution pattern also affects that of the glaciers' melt (Figure S5).

482 Within the regions spanning from the ELA to the zones of maximum snow accumulation (Batura: 4500-5400
483 m, Pasu: 4150-5400 m), glacier mass accumulated rapidly due to significantly heavy snowfall (Figure S5). Turbulent
484 heat exchange intensifies within this altitude range, with latent heat of melting melt energy approaching zero. A
485 modest amount of melting resulted in mass accumulation within the snowpack through refreezing (Figure S5). At
486 altitudes exceeding 5200 m, net radiation, turbulent exchange, and conductive heat flux did not demonstrate
487 significant variations. Net radiation was dominated by longwave radiation, and the snow's surface temperature
488 surpassed the air temperature. The glacier acted as an energy source, transferring energy to the atmosphere to sustain
489 maintain energy balance, ~~transferring energy to the atmosphere to maintain energy balance~~. While the maximum
490 snowfall on the Batura Glacier was similar to that on the Pasu Glacier, the accumulating area was larger. For instance,
491 in the region above 7000 m, up to 1 m w.e. of snowfall was observed on the Batura Glacier (Figures S5). Changes
492 in precipitation not only induced net radiation variations due to snow albedo feedback but also triggered outgoing
493 longwave radiation and sensible heat variations through alterations in surface temperature. This trait aligned with
494 some of the other glaciers in this area, as well as some glaciers in the West Kunlun and Pamir (Li et al., 2019; Zhu
495 et al., 2017; Bonekamp et al., 2019). However, the Batura Glacier exhibited more negative mass balance compared
496 to these glaciers including the Pasu glacier (The geodetic mass balance, as reported by Brun et al. (2017), is -0.01
497 ± 0.05 w.e.m yr⁻¹, while the simulated mass balance in this study is 0.01 ± 0.26 w.e.m yr⁻¹, both for the period from
498 2000 to 2016.).

499



500

501 **Figure 6-7** Characteristics of altitude gradient. Altitudinal distribution of the primary energy balance components

502

for (a) Batura Glacier and (b) Pasu glacier.

503

504 4.3 Impact of debris cover on glacier mass balance

505

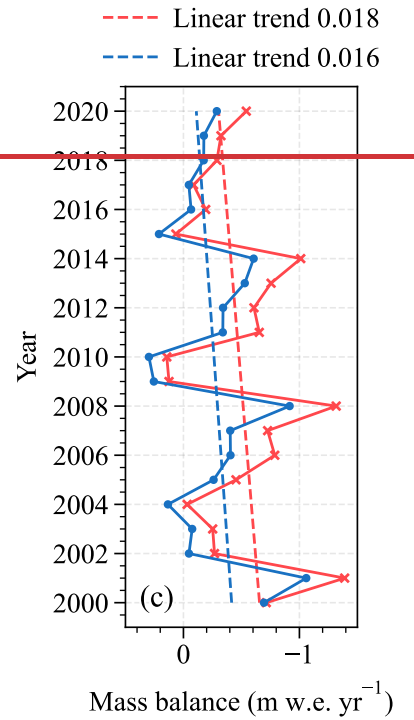
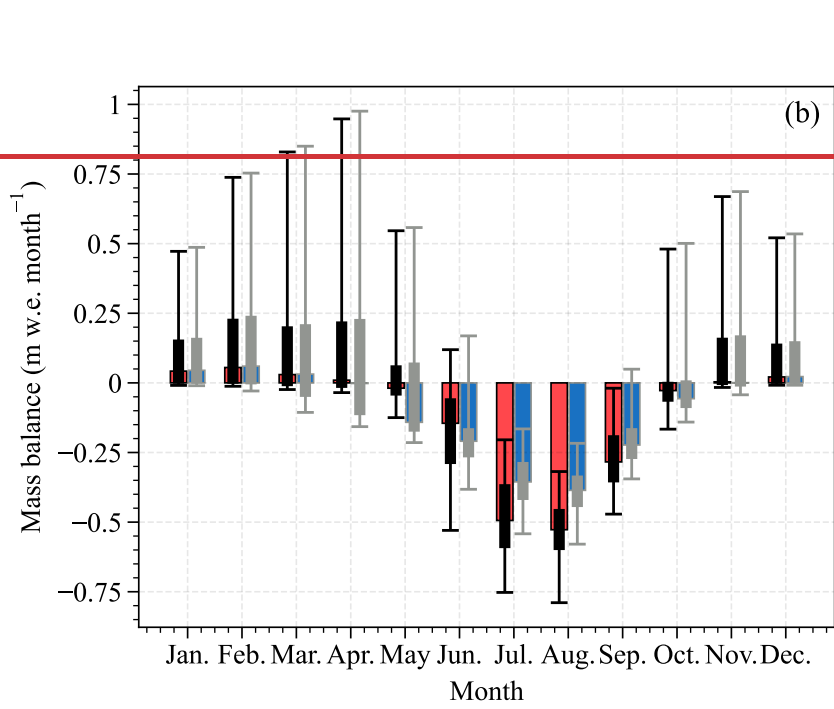
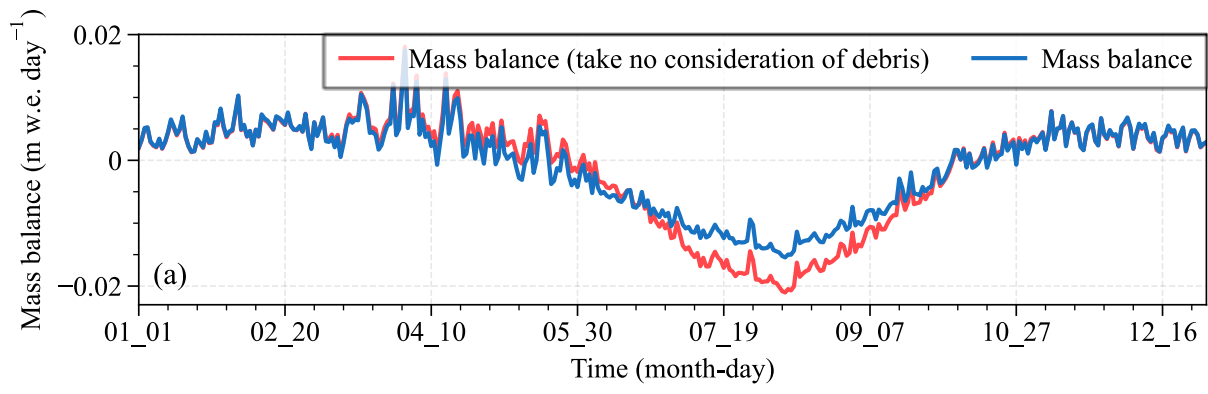
Our findings revealed that the presence of supraglacial debris led to a notable 45% reduction in negative mass

506 balance of the Batura Glacier. Specifically, in the absence of debris, the mass balance exhibited a value of -0.48 m
507 w.e. yr^{-1} , whereas with the inclusion of debris, this value decreased to $-0.26 \text{ m w.e. yr}^{-1}$, [likely due to the insulating](#)
508 [effect of debris on melt rate](#). ~~In contrast, a S~~ similar [modeling](#) experiments conducted in the Karakoram ~~demonstrated~~
509 [found](#) that the Baltoro Glacier experienced a reduction in ablation by approximately 35% when debris was excluded
510 (Groos et al., 2017). Moreover, glaciers in the Central Karakoram National Park, Pakistan, showed a 24%
511 decrease in [modeled](#) ablation when debris was excluded (Minora et al., 2015). ~~Collier et al. (2015) reported a~~
512 ~~proportion of ~14%~~. It's important to note that these ~~variations~~ [contrasting findings with respect to the impact of](#)
513 [debris cover on glacier mass balance in the Karakoram](#) can be attributed to differences in the models employed,
514 their configurations, and the thickness distribution of debris cover. The latter directly impacts the spatial
515 characteristics of sub-debris melting intensity (Compagno et al., 2022).

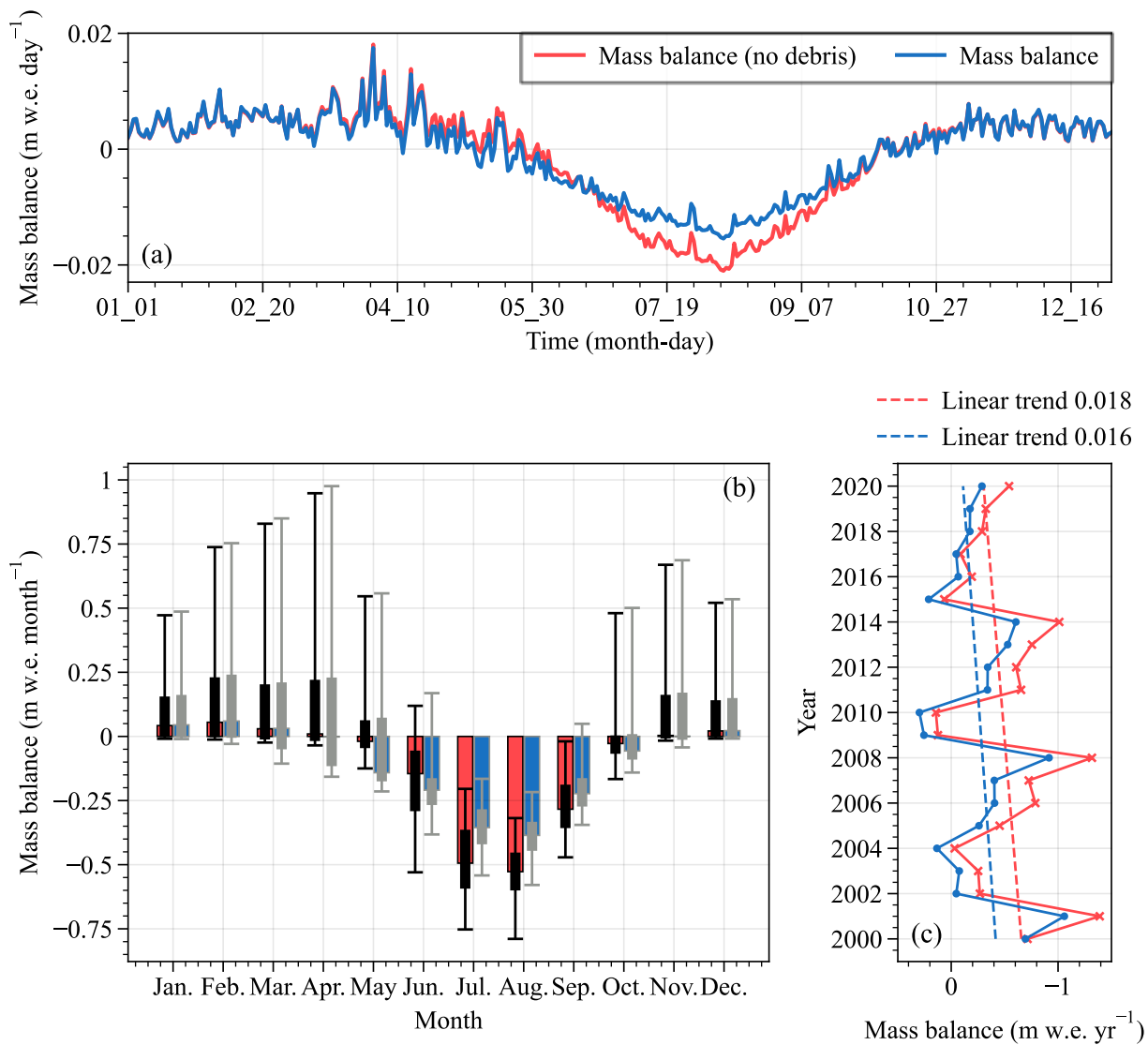
516 On a daily or monthly basis, the impact of supraglacial debris on the Batura Glacier manifested most
517 prominently during the ablation season, as depicted in Figure 8a and b. On an interannual scale, supraglacial debris
518 had a significant impact on mass balance of the Batura Glacier; however, it did not induce alterations in its overall
519 [temporal](#) fluctuations or trends (Figure ~~7e8c~~). This was mainly because the simulation process did not include the
520 influence of ~~changes in the debris cover distribution over time~~ [supraglacial debris evolution](#) on mass balance.

521 The debris had a significant protective effect, effectively mitigating glacier ablation. This effect was most
522 pronounced in August, a period characterized by high air temperatures. During May and June an extensive snow
523 cover blanketed the Batura Glacier. When supraglacial debris is included in energy balance processes, the snow
524 layer absorbed a greater amount of heat from the atmosphere through thermal conduction, thereby leading to
525 accelerated melting. As the snow progressively melted and the debris became exposed, the surface albedo
526 experienced a rapid decline spanning from July to October. This transition resulted in the debris absorbing a greater
527 portion of incoming shortwave radiation, much of which is returned to the atmosphere as emitted longwave radiation
528 ~~or~~ sensible heat, consequently yielding a reduction in the melting energy ~~affecting available the glacier~~ (Figure
529 ~~7b8b~~). Statistical analysis revealed that when supraglacial debris was not considered, the average net radiation
530 decreased by 14 W/m^2 . The most substantial reduction was observed in May, with a reduction of approximately 20
531 W/m^2 .

532



533



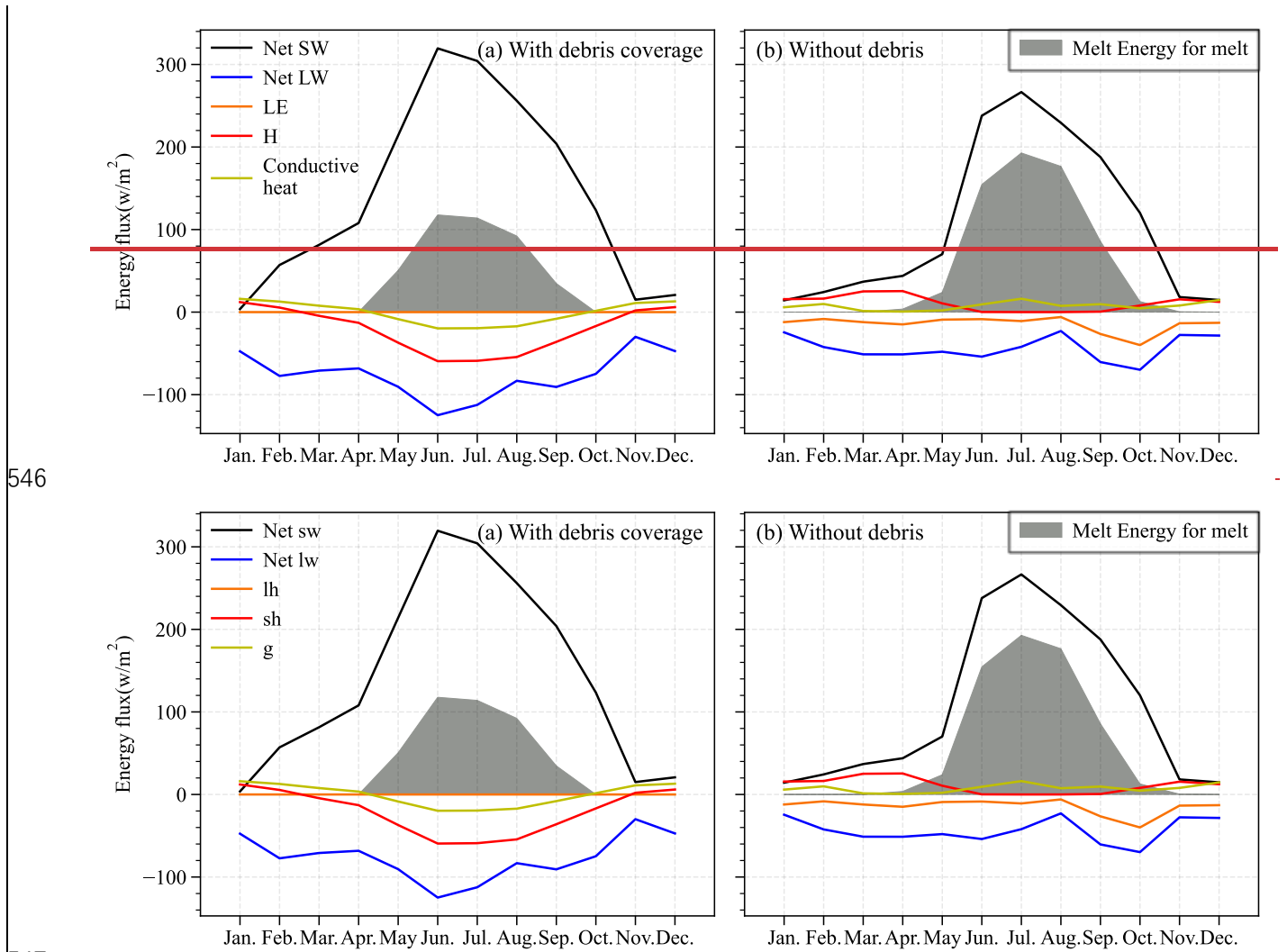
534

535 **Figure 7-8** The difference between modeled mass balance with (blue lines and bars) and without debris cover (red
 536 lines and bars): (a) daily mass balance; (b) monthly mass balance; and (c) annual mass balance trend.

537 4.4 The energy controls of sub-debris melt

538 We conducted additional investigations to understand how the supraglacial debris affect the ice ablation. In the
 539 case of the Batura Glacier, the presence of supraglacial debris reduces the average albedo of the glacier, thereby
 540 [fostering an augmented receipt of increasing](#) net shortwave radiation. Notwithstanding the observed augmentation
 541 in net radiation, an attenuation in melt was recorded. To investigate the impact of debris on energy-driven melting,
 542 this study conducted a statistical analysis of the energy balance for scenarios with and without debris coverage in
 543 the specific area characterized by the presence of debris (Figure 89). The results indicated that while the presence
 544 of debris did amplify the net radiation income, the available energy for melting is reduced by [the sum of](#) longwave

545 radiation emission, sensible heat, and thermal conduction within the debris (an average decrease of 25 W/m²).

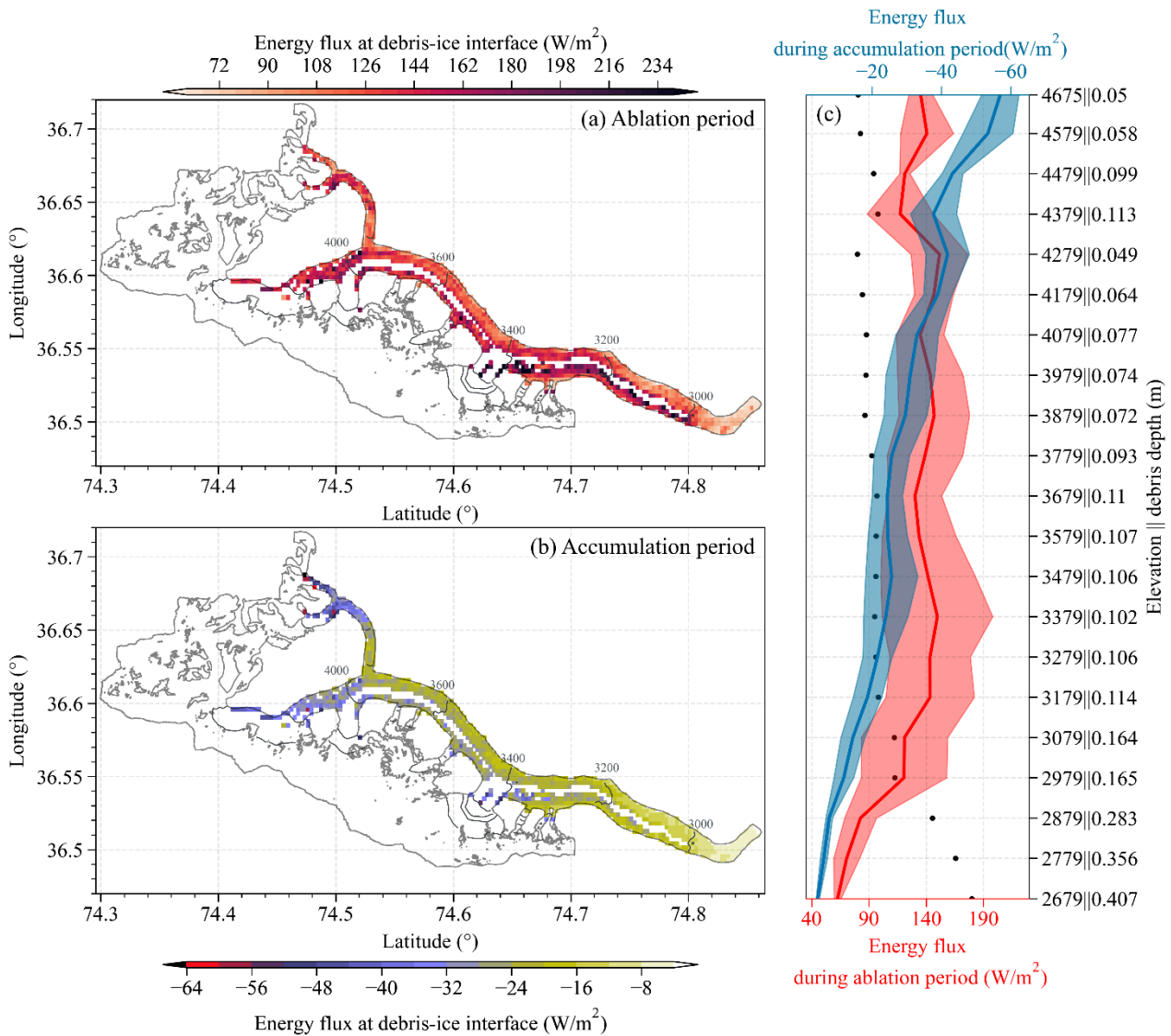


547
548 **Figure 8-9** Annual cycles of energy budget components (a) with and (b) without debris coverage for the currently
549 debris-covered area on Batura Glacier.

550 During the ablation season (June to September), when accounting for the presence of debris, the glacier's
551 energy income, represented by net shortwave radiation, witnessed an augmentation of 61 W/m². Meanwhile, the
552 energy output increased by 116 W/m², comprising net longwave radiation (50 W/m²), sensible heat (42 W/m²), and
553 conductive heat (24 W/m²). Consequently, this led to a reduction of 45 W/m² in latent heat of melt (sublimation heat
554 of the debris layer, which was not considered when deducting the 11 W/m² for sublimation heat without debris cover)
555 (Figure 8-9). In light of these observations, it can be concluded that the influence of debris cover on glacier melt is
556 twofold. Firstly, it perturbs-reverses the net direction of turbulent heat exchange processes on fluxes at the glacier
557 surface. Secondly, it alters the heat flux reaching the glacier through thermal conduction. The former aspect
558 primarily emanates from the heating of the debris layer due to shortwave radiation, causing the debris temperature

559 to surpass the atmospheric temperature. Consequently, the glacier transfers heat to the atmosphere, effectively acting
560 as an energy source. This finding aligns with earlier research results, as exemplified by Steiner et al. (2018) and
561 Nicholson and Stiperski (2020). Regarding the second aspect, we conducted an analysis that considered the thermal
562 conduction occurring within both the debris and ice layer, as well as the energy equilibrium within each layer. When
563 the [heat gained from](#) net radiation was conducted within the debris layers (the radiation penetration of the debris
564 was neglected), it could be consumed to heat the debris, thereby satisfying the energy balance within and between
565 the debris layers.

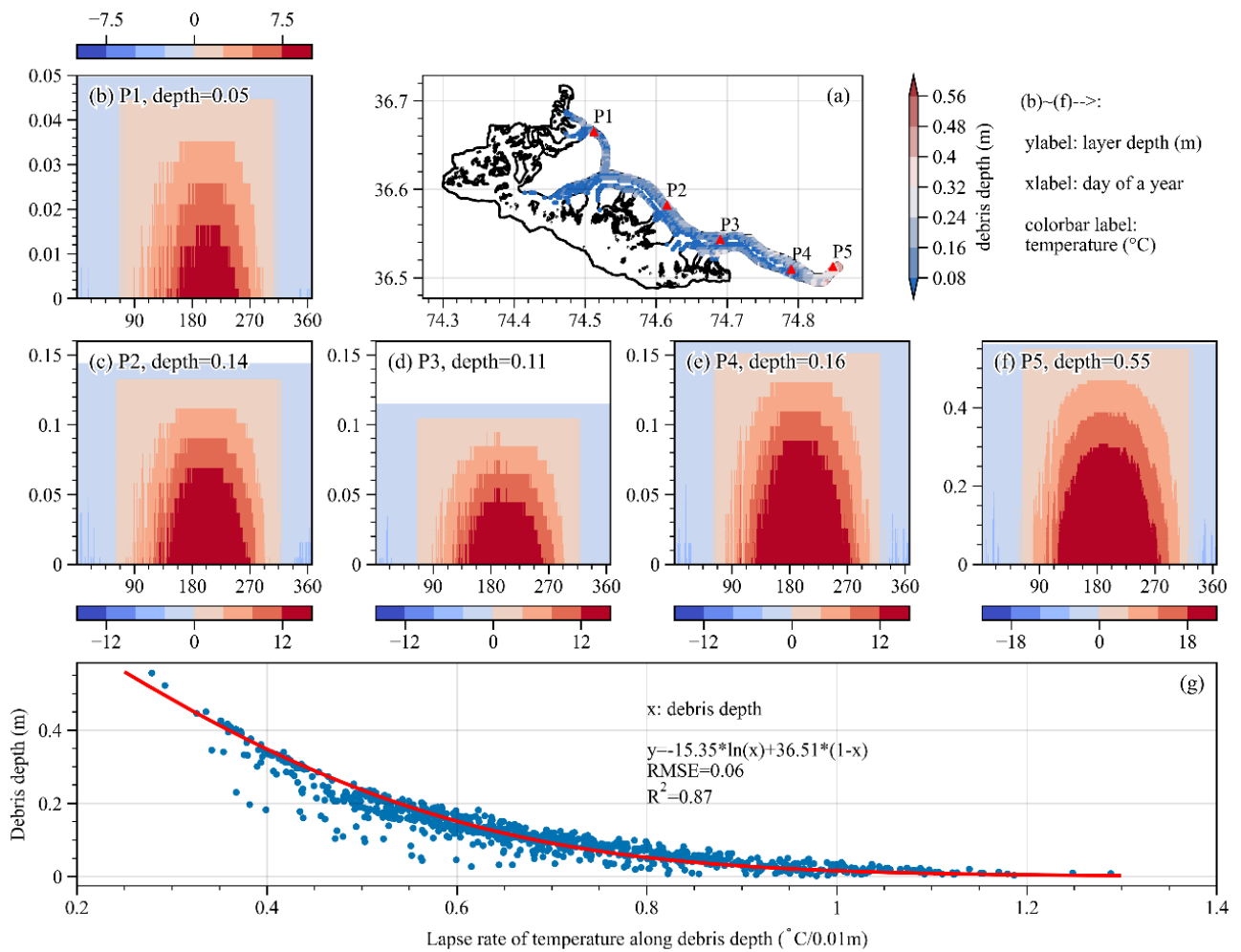
566 At the interface between debris and ice, heat exchange exhibits pronounced seasonal variations, with notable
567 altitudinal gradients, particularly during the accumulation period (Figure [910](#)). In the ablation season, a debris layer
568 is very quickly warmed by solar radiation before cooling back close to zero [after sunset](#). The temperature of surface
569 debris rises, transferring heat into the interior of the debris (Reid et al., 2012). However, the energy reaching the
570 debris-ice interface is predominantly influenced by the thickness of the debris layer. Below 2900 m, where the debris
571 thickness exceeds 20 cm, the energy at the debris-ice interface is less than 90 W/m². ~~As the altitude exceeds~~
572 [altitudes above 3200 m, and where](#) the debris thickness is less than 11 cm, the energy at the debris-ice interface
573 increases to 140 W/m² (Figure [910](#)). ~~Importantly, beyond an altitude of 3200 m, At these altitudes~~ the debris
574 thickness remains relatively constant, and correspondingly, the [energy flux at the](#) debris-ice interface
575 ~~maintain~~[exhibits](#) minor fluctuations. Despite Collier et al. (2015)'s suggestion that near-surface air temperature is
576 generally a stronger driver of melt rates below debris, our findings from the energy at the debris-ice interface, in
577 conjunction with Figure S6, imply that this relationship may not hold true during the ablation season in high-altitude
578 regions. During the accumulation season, the energy at the debris-ice interface is negative, with the glacier
579 transferring heat to the debris layer. This significantly affects the upwelling longwave radiation and sensible heat
580 flux at the debris surface. Thinner debris layers result in more heat transfer from the glacier to the debris (Figure
581 [9b10b](#)). In contrast to the ablation period, the energy at the debris-ice interface steadily increases with altitude during
582 the accumulation season. This difference may be attributed to snowfall causing substantial variations in the surface
583 energy balance process during the accumulation period compared to the ablation season. Overall, altitudes below
584 2900 m are identified as the less sensitive zone for Batura Glacier's ablation. ~~Concurrently~~[Conversely](#), the areas
585 where debris cover and bare ice intersect emerge as highly sensitive zones for melting, with the average thickness
586 of debris in these regions being less than 2.3 cm.



587
 588 **Figure 9-10** Spatial distribution of the mean energy flux at the debris-ice interface during ablation (a) and
 589 accumulation (b) periods. An elevation-dependent distribution of the debris-ice energy flux in each season is
 590 shown in (c).

591 The process of heat conduction within the debris was clearly illustrated in our study through an analysis of
 592 temperature changes within debris of varying thicknesses (Figure 10-11). During the ablation season, for thinner
 593 debris (Figure 10-11b, location P1), achieving a stable ice surface at absolute-zero $^{\circ}C$ necessitates a temperature
 594 difference of $2.5^{\circ}C$ within the uppermost 0.015 m (comprising 3 layers), with an average temperature decrease of
 595 $1.7^{\circ}C$ per 0.01 m increment. Conversely, in the case of thicker debris (Figure 10-11f), with a depth of 0.2 m (20
 596 layers), the temperature alteration amounts to $8^{\circ}C$, accompanied by a vertical temperature gradient of $0.4^{\circ}C$ per
 597 0.01 m increment. The variations in temperature are indicative of the attributes associated with sensible heat and
 598 conduction heat. Consequently, with respect to the upper layers, thin debris is more likely to conduct a greater

599 amount of heat. At the interface between glaciers-the surface ice and overlying supraglacial debris, the temperature
 600 change-difference at P1 (0.035-0.045 m) was 2.5 °C with a vertical gradient of 2.5 °C/0.01m. At P5 (0.42-0.55 m),
 601 the vertical gradient of temperature was 0.61 °C/0.01m (Figure 11). This indicates that in areas covered by thin
 602 supraglacial debris, more energy was transferred from the debris to the glacier, resulting in a greater amount of
 603 latent heat being released by the glacier.



604
 605 **Figure 10-11** Temporal variations of debris temperature across different depths throughout a year. Temperature
 606 profiles at specific points in (a) are displayed in (b)~(f). The relationship between temperature lapse rate and
 607 debris depth is presented in (g).

608 When the thickness of the debris is comparable, the vertical temperature gradient within the debris exhibits a
 609 corresponding similarity (P2, P4), except for slight deviations primarily observed at the surface. These variations
 610 are primarily attributed to discrepancies in both air temperature and surface temperature of the debris between the
 611 two points. Throughout the accumulation period, net shortwave radiation remained limited, leading to low
 612 temperatures and causing the debris temperature to either match-reach or drop below freezing point. As a result, the

613 rate of heat conduction process decelerated, thereby mitigating the influence of the debris on glacier melting.

614 To quantify the relationship between the thickness (x) of the debris layer and the vertical temperature gradient
615 (y), we computed the average temperature gradient for individual pixels within the debris-covered area during the
616 ablation period and conducted regression analysis (Figure 10g). According to Eq. 78, an increase in debris layer
617 thickness corresponds to a reduction in the vertical temperature gradient. Combined with Eq. 4 & 5, the heat
618 conduction to the interface between the debris layer and the glacier will also decrease, leading to diminished
619 availability of latent heat for glacier melting. As the thickness of the debris layer approaches minimal values, the
620 heat originating from a temperature difference of approximately 20°C is used for melting. This fundamentally
621 quantifies the impact of debris cover thickness on melt and further explains the differences in mass balance shown
622 in Figure S3S5.

$$623 \quad y = -15.35\ln(x) + 36.5(1 - x) \quad (78)$$

624

625 4.5 The potential uncertainties and limitations

626 The parameter settings significantly influence simulation results. Of ~~all the~~ six calibration parameters, the
627 simulation results are highly sensitive to firn albedo, ice roughness length, and debris albedo (Figure S1 and S3).
628 The ~~most significant~~ largest changes are observed when varying the debris albedo. When the debris albedo decreases
629 to 0.1 (approximately a 2-3% change in albedo from the calibrated value), the melt increases by about 3.4%. With
630 a ~~5100%~~ increase in debris albedo (0.26), the melt decreases by approximately 14%. This magnitude of sensitivity
631 is consistent with the findings of Giese et al. (2020) on Changri Nup Glacier in the Himalayas. The calibrated
632 parameters ice and firn roughness length lie on the margin of the range, implying that a larger range may be
633 beneficial or that a parameter not considered in calibration is not chosen optimally. However, extending the limits
634 of these parameters would result in physically unrealistic values. Due to the complexity of the model, we did not
635 calibrate all parameters. Instead, we identified the aforementioned six parameters through sensitivity analysis.
636 Besides the calibrated parameters, certain factors, such as the rain and snow separation threshold, ~~continue to~~
637 influence the simulated mass balance. In this study, we constrained these parameters using geodetic mass balance.

638 Apart from the model-inherent parameters, the model's input dataset presents considerable challenges during
639 calibration and introduces uncertainty into the results (Arndt and Schneider, 2023). While HAR data has been
640 applied in glacier mass balance simulation studies (e.g., Huintjes et al. (2015b) and Groos et al. (2017)), its
641 applicability in the Karakoram mountains remains uncertain~~ies~~ (Groos et al., 2017) due to the majority of ground

642 validation being conducted on the Tibetan Plateau (Maussion et al., 2014). Additionally, uncertainties can also be
643 introduced by the calibration methods and downscaling schemes of the climatic factors, as evident from the
644 comparison of our study with results from Groos et al. (2017). Initially, Groos et al. (2017) downscaled HAR Version
645 1 data to 30 m resolution using interpolation for glacier mass balance simulations in the Karakoram. In this study,
646 we first calibrated temperature and precipitation in HAR Version 2 using station observations and then employed
647 statistical downscaling to achieve a 300m resolution for energy balance research, incorporating radiative
648 downscaling that accounts for complex topography. While both results of Groos et al. (2017) and this study compare
649 well with station observations, discrepancies exist in temperature and precipitation on Batura Glacier. For example,
650 Groos et al. (2017) reported a temperature of 5.0 °C during the ablation season at ~4,060 m a.s.l., while this study
651 recorded 1.7°C at the same elevation. Annual precipitation for Batura Glacier is ~960 mm in this study compared
652 to 1059 mm in Groos et al. (2017). These differences resulted in significant spatial disparities between the two
653 simulated results (Figure 5a of this study and Figure 6 of Groos et al. (2017)). Although the multi-year average mass
654 balance in this study aligns more closely with geodetic mass balance compared with that of Groos et al. (2017), it
655 remains challenging to determine which result can better capture the spatial characteristics of glacier mass balance
656 due to a lack of knowledge about meteorological conditions in high-altitude glacierized regions and insufficient
657 characterization of surface features like ice cliffs and supraglacial ponds in both models. Therefore, as highlighted
658 by Collier et al. (2013), this uncertainty can only be minimized through additional high-altitude observations and
659 more reliable downscaling approaches, such as dynamic downscaling.

660 The spatial resolution of a glacier model can impact simulation results, particularly in debris-covered areas. To
661 investigate this effect, we conducted comparative simulations with varying resolutions on a small section of the
662 Batura Glacier terminus. We used the 300 m resolution simulation from this study as the benchmark. When
663 increasing the resolution to 100 m (matching the debris data resolution), the average debris thickness showed a
664 minimal difference of 0.01 m compared to the 300 m resolution thickness. However, the spatial distribution of debris
665 thickness exhibited significant discrepancies, especially at the glacier margins (Figure S7a, b). Notably, subsurface
666 melt rate decreased by 2.2% compared to the benchmark (Figure S7e). Since debris albedo was set as a constant
667 value, net radiation remained relatively unchanged. However, the surface temperature decreased by 0.17°C (Figure
668 S7f), accompanied by a 1.9% reduction in sensible heat flux (Figure S7i) and a 2.7% decrease in conductive heat
669 transfer within the debris layer (Figure S7j). These findings demonstrate that while spatial resolution influences the
670 energy fluxes and ablation of debris-covered glaciers, its primary impact lies in the spatial distribution (Figure S7c,

671 d) with minimal effect on average values. This spatial variation primarily stems from the differences in debris
672 thickness captured at varying resolutions. Given the limitations of the employed debris thickness data (Rounce et
673 al., 2021), we cannot definitively conclude if higher resolution simulations yield results closer to reality.
674 Additionally, the computational cost of high-resolution simulations is substantial. Therefore, this study utilized a
675 coarser grid to capture the overall energy and mass balance characteristics of the glacier. However, the potential for
676 more realistic outcomes with reliable high-resolution debris thickness data is undeniable.

677 The main limitation of the model lies in the absence of parameterization for the impact of glacier surface
678 features on melting, such as ice cliffs and supraglacial ponds. This omission may lead to an underestimation of the
679 ice melt rate across debris-covered areas, as observed amplifying effects of supraglacial lakes and ice cliffs on
680 glacial melt (e.g., Tedesco et al. (2012), Miles et al. (2016), and Buri et al. (2021)) are not considered. Supraglacial
681 ponds and lakes efficiently transfer heat into glacier ice due to their low surface albedo and active convection.
682 Simulations by Miles et al. (2018) indicated that ponds may contribute to 1/8 of total ice loss in the Langtang Valley,
683 Nepal. Modeling by Huo et al. (2021a) also suggested a substantial increase in ice loss on the Baltoro Glacier in the
684 Karakoram due to the intervention of supraglacial ponds. Supraglacial ice cliffs influence glacier ice melt by creating
685 a direct ice-atmosphere interface with low albedo and exposure to high emissions of longwave radiation from
686 surrounding debris-covered surfaces (Buri et al., 2016). According to Buri et al. (2021), neglecting ice cliffs in
687 Langtang Valley would result in a mass loss underestimation of $17\% \pm 4\%$ for debris-covered glacier tongues. In
688 most glaciers, interactions generally exist between ice cliffs and ponds/lakes (Buri et al., 2021; Huo et al., 2021a).
689 Therefore, future research should incorporate parameterization for these elements to better understand their impact
690 on glacier melting. However, in the absence of sufficient observations, a limited representation of ponds and ice
691 cliffs in the parameterization of model can introduce additional uncertainty in glacier-wide energy fluxes (Miles et
692 al., 2016).

693

694 5 Conclusions and outlook

695 This study presented a comprehensive investigation into the relationships between supraglacial debris cover,
696 energy fluxes, and mass balance dynamics on the Batura Glacier in the Karakoram. Through simulation analysis,
697 we propose that the presence of debris on the glacier surface effectively reduces the amount of latent heat available
698 for ablation by absorbing solar radiation and preventing it from reaching the ice surface, which creates a favorable
699 condition for the Batura Glacier's relatively low negative mass balance. ~~we propose that the primary factor~~

700 ~~influencing the comparatively low negative mass balance of the Batura Glacier is the substantial inhibitory impact~~
701 ~~exerted by the surface debris on the process of ablation.~~ Furthermore, the glacier's mass budget has shown a
702 decreasing trend in [\(negative\)](#) magnitude between 2000 and 2020, primarily due to a reduction in ablation, especially
703 in areas with thin debris cover and debris-free parts of the ablation area, which outweighs the relatively smaller
704 reduction in snowfall accumulation. More detailed findings and [viewpoints-outcomes](#) of the study are concluded as
705 follows.

706 (1) The Batura Glacier exhibits substantial spatial heterogeneity in mass balance distribution along its
707 elevation gradient. Altitudinal dependence was influenced by the presence of debris cover, resulting in the
708 most intense melting occurring between 3000 and 3400 m, with a reversal of the ablation gradient below
709 3000 m due to the greater insulation by thicker debris on the lower portion of the glacier.

710 (2) Our simulations revealed that supraglacial debris cover exerted a notable influence on glacier mass balance.
711 Including debris cover in the energy balance model led to a 45% reduction in the [overall-magnitude of the](#)
712 [negative](#) mass balance of the Batura Glacier (with debris: -0.26 m w.e. yr^{-1} , without debris: -0.48 m w.e.
713 yr^{-1}). This reduction was particularly prominent during the ablation season, highlighting the significance
714 of debris cover in mitigating glacier ablation.

715 (3) The role of debris cover in altering energy exchange was multifaceted. Debris cover enhances net radiation
716 income by reducing albedo but also promotes thermal transfer, which warms the debris and leads to a
717 higher rate of energy transfer to the atmosphere through longwave emission and sensible heat, thereby
718 ~~moderating latent heat of melting~~[reducing available melt energy compared with bare ice](#). This intricate
719 interplay modified the glacier's response to energy budgets, ultimately affecting its mass balance.

720 (4) Our investigation into the effects of debris thickness on temperature gradients within the debris layer
721 reveals a fundamental connection between debris thickness and its influence on melt processes. Thicker
722 debris layers engender reduced temperature gradients, leading to reduced latent heat available for glacier
723 melting.

724 This study significantly advances our understanding of energy and mass interaction on debris-covered glaciers
725 in the Karakoram. However, in addition to the previously discussed impact of ponds and ice-cliffs on ice ablation,
726 future work should also address the evolution of supraglacial debris thickness and glacier dynamics. These factors
727 exert a significant influence on the energy reaching the glacier surface (Compagno et al., 2022; Huo et al., 2021b).
728 Finally, this paper ~~has pointed out~~[identified](#) that the mass balance of Batura Glacier ~~is-becameing~~ less negative [in](#)

729 [the period 2000-2020, most likely due to a decrease in air temperature over the same period. This result supports](#)
730 [wider findings associated](#)~~which is an interesting phenomenon linking~~ with the "Karakoram anomaly" and [this](#)
731 [phenomenon](#) ~~should be~~[warrants](#) further discussion [on](#) and investigation.

732

733 **Declaration of competing interest**

734 The contact author has declared that none of the authors has any competing interests.

735

736 **Data/Code availability**

737 HAR dataset is available from Institute of Ecology Chair of Climatology website at [https://www.klima.tu-](https://www.klima.tu-berlin.de/index.php?show=daten_har2&lan=en)
738 [berlin.de/index.php?show=daten_har2&lan=en](https://www.klima.tu-berlin.de/index.php?show=daten_har2&lan=en). Meteorology and ablation observations. Glacier surface elevation
739 difference of Wu et al. (2021) is available upon request from the authors, the elevation difference produced by
740 Hugonnet et al. (2021), Shean et al. (2020), and Brun et al. (2017) are available at <https://doi.org/10.6096/13.>, from
741 National Snow and Ice Data Center (NSIDC) at <https://nsidc.org/data/highmountainasia> and from PANGAEA
742 website at <https://doi.pangaea.de/10.1594/PANGAEA.876545>. The KGI datasets are available from the National
743 Cryosphere Desert Data Center of China at <https://doi.org/10.12072/ncdc.glacier.db2386.2022>. The observations
744 collected by this research are available upon reasonable request from the authors. The COSIPY used in this study is
745 available on GitHub at <https://github.com/cryotools/cosipy>. The code developed for calculating energy and mass
746 balance on supraglacial debris is available upon request from the authors. The coupled model will be publicly
747 available once some technical issues are fixed.

748

749 **Author contribution**

750 Yu Zhu: Conceptualization, [m](#)Methodology, [m](#)Model development, [w](#)Writing original draft, [w](#)Writing review &
751 editing. Shiyin Liu: Conceptualization, [s](#)supervision, [p](#)Project administration, [f](#)funding acquisition. Ben W. Brock:
752 Supervision, [m](#)Model development, [w](#)Writing review & editing. Lide Tian: Supervision, [p](#)Project administration.
753 Ying Yi: Validation, [f](#)Formal analysis, [w](#)Writing original draft. Fuming Xie: Investigation, [v](#)Visualization. Donghui
754 Shangguan: Investigation. Yiyuan Shen: Formal analysis, [v](#)Visualization.

755

756 **Acknowledgments**

757 The authors acknowledge financial support from the National Natural Science Foundation of China (Nos. 42301154
758 and 42171129), the National Key R&D Program International Science and Technology Innovation Cooperation
759 Project (No. 2023YFE0102800), and the Postdoctoral Research Foundation of Yunnan Province (No.
760 C615300504038). The authors express gratitude to Water and Power Development Authority (WAPDA) for
761 contributing their meteorological data and debris thickness observations. Special thanks to Professor Tobias Sauter
762 and his team for open-sourcing the COSIPY model. We also thank an anonymous reviewers and Dr. Alexander
763 Raphael Groos for helpful comments and suggestions on this manuscript.

764

765 **Appendix A Correction and downscaling of the model Inputs**

766 **A1 Adjusting of precipitation**

767 Numerous research endeavors have elucidated notable biases in precipitation observations within and in the
 768 vicinity of the Hunza river basin. For instance, Winiger et al. (2005) discovered a noteworthy discrepancy, with
 769 precipitation at altitudes surpassing 5000 m exhibiting sixfold or more intensity compared to lower altitudes, as
 770 deduced from station observations. Similarly, Tahir et al. (2011) ascertained a dissimilarity between runoff and
 771 observed precipitation, with Dainyor station recording a runoff of 750 mm/yr but a mere 100 mm/yr of observed
 772 precipitation. This asymmetry was also discerned in the neighboring region (Immerzeel et al., 2009). To make a
 773 more accurate precipitation input for the simulation, we consulted the method proposed by Wortmann et al. (2018)
 774 to rectify the precipitation data. This method entails the calibration of precipitation through the calculation of the
 775 calibration factor $f_c(H)$, as expressed by the following equation:

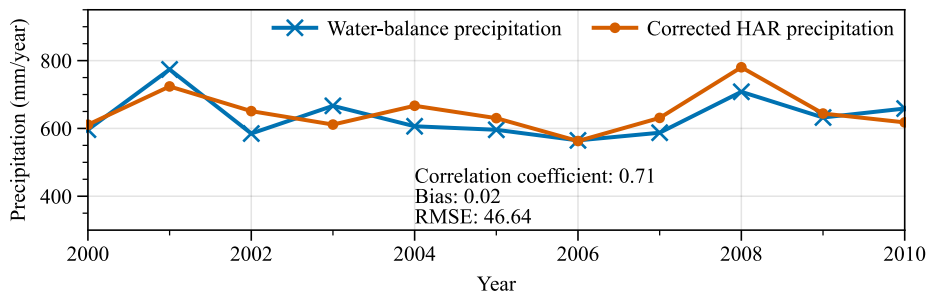
776
$$f_c(H) = (c - 1) \exp \left\{ - \left[\frac{P_{LR}}{(c-1)*100} \right]^2 * (H - H_{max})^2 \right\} + 1 \quad (A1)$$

777 Where c represents the calibration factor, H_{max} represents the maximum elevation at which precipitation
 778 occurs, P_{LR} signifies the elevation correction factor for precipitation. These parameters are determined using the
 779 linear relationship proposed by Immerzeel et al. (2012), and the range of values for the determination is derived
 780 from existing studies. The linear relationship can be expressed as follows:

781
$$\begin{cases} P_T = P_{HAR} * [1 + (H - H_{ref}) * P_{LR} * 0.01] & H_{ref} < H < H_{max} \\ P_T = P_{HAR} * [1 + ((H_{max} - H_{ref}) + (H_{max} - H)) * P_{LR} * 0.01] & H > H_{max} \end{cases} \quad (A2)$$

782 Where H_{ref} denotes the reference elevation, which corresponds to the elevation at which the observed
 783 precipitation closely matches the actual precipitation. P_{HAR} and P_T represent HAR precipitation and calibrated
 784 precipitation. We determined H_{max} and P_{LR} by approximating the calculated P_r based on the water balance
 785 equation (Eq. A3) (Figure A1), with the range of values for H_{max} and P_{LR} referencing the priori studies. In the
 786 Eq.3, ET uses MODIS evapotranspiration products, R takes the runoff from the watershed outlet observation
 787 station (Dainyor station), and TWS takes the average of GLDAS and GRACE ~~solutions~~solutions.

788
$$P_r - ET - R - TWS = 0 \quad (A3)$$



789

790 **Figure A1** Comparison between corrected precipitation and precipitation calculated by water balance equation.

791 **A2 Downscaling of the model inputs**

792 In order to achieve the desired level of precision for mass balance simulation on a glacier scale, this study
793 downscaled HAR reanalysis data from 10 km to 300 m by using statistical methods. Special attention was given to
794 the impacts of topography, slope, and aspect on meteorological factors during this process. The SRTM DEM with a
795 spatial resolution of approximately 30 meters was utilized to obtain topographic features. In order to effectively
796 represent topographical features on a glacier scale while maintaining optimal computational efficiency during the
797 energy balance simulation process, the target grid size was set at 10 times the SRTM DEM (~300 m).

798 Based on water balance at basin outlet, the precipitation was first calibrated using remote sensing data and
799 station observations to obtain the altitude gradient ~~lapse-rate~~ and maximum precipitation altitude (Supplementary
800 Methods). After calibration, the altitude gradient ~~lapse-rate~~ of precipitation throughout the Hunza river basin was
801 determined to be 0.18%/m. The maximum precipitation altitude of the Batura glacier was 4900 m. Then, the
802 precipitation was downscaled at a resolution of 300 m for the Batura glacier by applying the Eq.1 provided in the
803 Supplementary. Incoming shortwave radiation was downscaled by using the radiative transfer equation (Eq.4) on
804 sloping surfaces. The details in solving this equation can be found in publication of Ham (2005). The correlation
805 coefficient of incoming shortwave radiation before and after downscaling is 0.91, with an RMSE of 26, indicating
806 the parameterization-based downscaling enables a more refined representation of spatial characteristics while
807 preserving the original characteristics and trends of the data.

$$808 \quad R_{gs} = R_b \left(\frac{\cos(\phi) \cos(i) + \sin(\phi) \sin(i) \cos(\gamma - \alpha)}{\cos(\phi)} \right) + R_d \quad (4)$$

809 In the above equation, R_d represents scattered radiation, which is solved using a modified Gompertz function
810 that quantifies the relationship between horizontal total radiation (R_{gh}) and clear sky index (CI) (Wohlfahrt et al.,
811 2016); CI is determined based on radiation duration, while R_{gh} is initialized as R_{gs} ; R_b denotes direct incident
812 radiation and is calculated by subtracting R_d from R_{gh} ; ϕ and γ represent solar zenith angle and azimuth angle
813 respectively, which can be obtained using parameterization schemes proposed by Wohlfahrt et al. (2008); i denotes
814 the angle between the slope and horizontal plane, while α represents the azimuth angle of the slope.

815 Temperature, relative humidity, wind speed, and air pressure were downscaled using altitude gradient ~~lapse-rates~~
816 obtained from HAR data. Cloud cover was downscaled refer to the scheme of ERA5 (Muñoz Sabater, 2019). Owing
817 to the absence of meteorological observations required for computing altitude gradient ~~lapse-rates~~, the altitude
818 gradient ~~lapse-rates~~ over a broader region (Karakoram Mountains), which encompasses the study area, were

819 determined using HAR data to minimize errors. The altitude gradient ~~lapse rate~~ for 2 m air temperature was
820 calculated to be -0.0054 °C/m, while that for 2 m wind speed was 0.00078 m*s⁻¹/m. The rate for 2 m relative
821 humidity was 0.014 %/m, and that for atmospheric pressure was -0.044 hPa/m.

822

823

824 References

825 Agarwal, V., Bolch, T., Syed, T. H., Pieczonka, T., Strozzi, T., and Nagaich, R.: Area and mass changes of Siachen
826 Glacier (East Karakoram), *Journal of Glaciology*, 63, 148-163, 10.1017/jog.2016.127, 2016.

827 Allen, R., Pereira, L., Raes, D., Smith, M., Allen, R. G., Pereira, L. S., and Martin, S.: Crop Evapotranspiration:
828 Guidelines for Computing Crop Water Requirements, FAO Irrigation and Drainage Paper 56, FAO, 56, 1998.

829 Arndt, A. and Schneider, C.: Spatial pattern of glacier mass balance sensitivity to atmospheric forcing in High
830 Mountain Asia, *Journal of Glaciology*, 1-18, 10.1017/jog.2023.46, 2023.

831 Azam, M. F., Wagnon, P., Berthier, E., Vincent, C., Fujita, K., and Kargel, J. S.: Review of the status and mass changes
832 of Himalayan-Karakoram glaciers, *Journal of Glaciology*, 64, 61-74, 10.1017/jog.2017.86, 2018.

833 Banerjee, A.: Brief communication: Thinning of debris-covered and debris-free glaciers in a warming climate, *The
834 Cryosphere*, 11, 133-138, 10.5194/tc-11-133-2017, 2017.

835 Basnett, S., Kulkarni, A. V., and Bolch, T.: The influence of debris cover and glacial lakes on the recession of glaciers
836 in Sikkim Himalaya, India, *Journal of Glaciology*, 59, 1035-1046, 10.3189/2013JoG12J184, 2013.

837 Bhambri, R., Hewitt, K., Kawishwar, P., and Pratap, B.: Surge-type and surge-modified glaciers in the Karakoram,
838 *Sci Rep*, 7, 15391, 10.1038/s41598-017-15473-8, 2017.

839 Bintanja, R. and Van, D. B., Michiel R.: The Surface Energy Balance of Antarctic Snow and Blue Ice, *Journal of
840 Applied Meteorology*, 34, 902-926, 1995.

841 Bisset, R. R., Dehecq, A., Goldberg, D. N., Huss, M., Bingham, R. G., and Gourmelen, N.: Reversed Surface-Mass-
842 Balance Gradients on Himalayan Debris-Covered Glaciers Inferred from Remote Sensing, *Remote Sensing*, 12,
843 10.3390/rs12101563, 2020.

844 Bolch, T., Pieczonka, T., Mukherjee, K., and Shea, J.: Brief communication: Glaciers in the Hunza catchment
845 (Karakoram) have been nearly in balance since the 1970s, *The Cryosphere*, 11, 531-539, 10.5194/tc-11-531-2017,
846 2017.

847 Bolton, D.: The Computation of Equivalent Potential Temperature, *Monthly Weather Review*, 108, 1046-1053, 1980.

848 Bonekamp, P. N. J., de Kok, R. J., Collier, E., and Immerzeel, W. W.: Contrasting Meteorological Drivers of the Glacier
849 Mass Balance Between the Karakoram and Central Himalaya, *Frontiers in Earth Science*, 7,
850 10.3389/feart.2019.00107, 2019.

851 Brun, F., Berthier, E., Wagnon, P., Kaab, A., and Treichler, D.: A spatially resolved estimate of High Mountain Asia
852 glacier mass balances, 2000-2016, *Nat Geosci*, 10, 668-673, <https://doi.org/10.1038/NGEO2999>, 2017.

853 Buri, P., Miles, E. S., Steiner, J. F., Ragettli, S., and Pellicciotti, F.: Supraglacial Ice Cliffs Can Substantially Increase the
854 Mass Loss of Debris-Covered Glaciers, *Geophysical Research Letters*, 48, 10.1029/2020gl092150, 2021.

855 Buri, P., Miles, E. S., Steiner, J. F., Immerzeel, W. W., Wagnon, P., and Pellicciotti, F.: A physically based 3-D model
856 of ice cliff evolution over debris-covered glaciers, *Journal of Geophysical Research: Earth Surface*, 121, 2471-2493,
857 10.1002/2016jf004039, 2016.

858 Collier, E., Maussion, F., Nicholson, L. I., Mölg, T., Immerzeel, W. W., and Bush, A. B. G.: Impact of debris cover on
859 glacier ablation and atmosphere-glacier feedbacks in the Karakoram, *The Cryosphere*, 9, 1617-1632, 10.5194/tc-
860 9-1617-2015, 2015.

861 Collier, E., Mölg, T., Maussion, F., Scherer, D., Mayer, C., and Bush, A. B. G.: High-resolution interactive modelling
862 of the mountain glacier–atmosphere interface: an application over the Karakoram, *The Cryosphere*, 7, 779–795,
863 10.5194/tc-7-779-2013, 2013.

864 Collier, E., Nicholson, L. I., Brock, B. W., Maussion, F., Essery, R., and Bush, A. B. G.: Representing moisture fluxes
865 and phase changes in glacier debris cover using a reservoir approach, *The Cryosphere*, 8, 1429–1444, 10.5194/tc-
866 8-1429-2014, 2014.

867 Compagno, L., Huss, M., Miles, E. S., McCarthy, M. J., Zekollari, H., Dehecq, A., Pellicciotti, F., and Farinotti, D.:
868 Modelling supraglacial debris-cover evolution from the single-glacier to the regional scale: an application to High
869 Mountain Asia, *The Cryosphere*, 16, 1697–1718, 10.5194/tc-16-1697-2022, 2022.

870 Curio, J., Maussion, F., and Scherer, D.: A 12-year high-resolution climatology of atmospheric water transport over
871 the Tibetan Plateau, *Earth System Dynamics*, 6, 109–124, 10.5194/esd-6-109-2015, 2015.

872 Dimri, A. P.: Decoding the Karakoram Anomaly, *Sci Total Environ*, 788, 147864, 10.1016/j.scitotenv.2021.147864,
873 2021.

874 Evatt, G. W., Abrahams, I. D., Heil, M., Mayer, C., Kingslake, J., Mitchell, S. L., Fowler, A. C., and Clark, C. D.: Glacial
875 melt under a porous debris layer, *Journal of Glaciology*, 61, 825–836, 10.3189/2015JoG14J235, 2015.

876 Forsythe, N., Fowler, H. J., Li, X.-F., Blenkinsop, S., and Pritchard, D.: Karakoram temperature and glacial melt driven
877 by regional atmospheric circulation variability, *Nature Climate Change*, 7, 664–670, 10.1038/nclimate3361, 2017.

878 Fujita, K. and Sakai, A.: Modelling runoff from a Himalayan debris-covered glacier, *Hydrology and Earth System
879 Sciences*, 18, 2679–2694, 10.5194/hess-18-2679-2014, 2014.

880 Gao, H., Zou, X., Wu, J., Zhang, Y., Deng, X., Hussain, S., Wazir, M. A., and Zhu, G.: Post-20(th) century near-steady
881 state of Batura Glacier: observational evidence of Karakoram Anomaly, *Sci Rep*, 10, 987, 10.1038/s41598-020-
882 57660-0, 2020.

883 Gardelle, J., Berthier, E., and Arnaud, Y.: Slight mass gain of Karakoram glaciers in the early twenty-first century,
884 *Nature Geoscience*, 5, 322–325, 10.1038/ngeo1450, 2012.

885 Giese, A., Boone, A., Wagnon, P., and Hawley, R.: Incorporating moisture content in surface energy balance
886 modeling of a debris-covered glacier, *The Cryosphere*, 14, 1555–1577, 10.5194/tc-14-1555-2020, 2020.

887 Groos, A. R., Mayer, C., Smiraglia, C., Diolaiuti, G., and Lambrecht, A.: A first attempt to model region-wide glacier
888 surface mass balances in the Karakoram: findings and future challenges, *Geografia fisica e dinamica quaternaria*,
889 40, 137–159, 2017.

890 Ham, J. M.: Useful Equations and Tables in Micrometeorology, in: *Micrometeorology in Agricultural Systems*, 533–
891 560, <https://doi.org/10.2134/agronmonogr47.c23>, 2005.

892 Hasson, S., Böhner, J., and Lucarini, V.: Prevailing climatic trends and runoff response from Hindukush–Karakoram–
893 Himalaya, upper Indus Basin, *Earth System Dynamics*, 8, 337–355, 10.5194/esd-8-337-2017, 2017.

894 Herron, M. M. and Langway, C. C.: Firn Densification: An Empirical Model, *Journal of Glaciology*, 25, 373–385,
895 10.3189/S0022143000015239, 1980.

896 Hewitt, K.: The Karakoram Anomaly? Glacier Expansion and the ‘Elevation Effect,’ Karakoram Himalaya, *Mountain
897 Research and Development*, 25, 332–340, 10.1659/0276-4741(2005)025[0332:tkagea]2.0.co;2, 2005.

898 Hoffman, M. J., Fountain, A. G., and Liston, G. E.: Distributed modeling of ablation (1996–2011) and climate
899 sensitivity on the glaciers of Taylor Valley, Antarctica, *Journal of Glaciology*, 62, 215–229, 10.1017/jog.2015.2, 2016.

900 Hugonnet, R., McNabb, R., Berthier, E., Menounos, B., Nuth, C., Girod, L., Farinotti, D., Huss, M., Dussailant, I., Brun,
901 F., and Kaab, A.: Accelerated global glacier mass loss in the early twenty-first century, *Nature*, 592, 726–731,
902 <https://doi.org/10.1038/s41586-021-03436-z>, 2021.

903 Huintjes, E.: Energy and mass balance modelling for glaciers on the Tibetan Plateau : extension, validation and
904 application of a coupled snow and energy balance model, RWTH Aachen University, 2014.

905 Huintjes, E., Neckel, N., Hochschild, V., and Schneider, C.: Surface energy and mass balance at Purogangri ice cap,
906 central Tibetan Plateau, 2001–2011, *Journal of Glaciology*, 61, 1048–1060, 10.3189/2015JoG15J056, 2015a.

907 Huintjes, E., Sauter, T., Schröter, B., Maussion, F., Yang, W., Kropáček, J., Buchroithner, M., Scherer, D., Kang, S., and
908 Schneider, C.: Evaluation of a Coupled Snow and Energy Balance Model for Zhadang Glacier, Tibetan Plateau,
909 Using Glaciological Measurements and Time-Lapse Photography, *Arctic, Antarctic, and Alpine Research*, 47, 573–
910 590, 10.1657/aaar0014-073, 2015b.

911 Huo, D., Bishop, M. P., and Bush, A. B. G.: Understanding Complex Debris-Covered Glaciers: Concepts, Issues, and
912 Research Directions, *Frontiers in Earth Science*, 9, 10.3389/feart.2021.652279, 2021a.

913 Huo, D., Bishop, M. P., Young, B., and Chi, Z.: Modeling the feedbacks between surface ablation and morphological
914 variations on debris-covered Baltoro Glacier in the central Karakoram, *Geomorphology*, 389,
915 10.1016/j.geomorph.2021.107840, 2021b.

916 Immerzeel, W. W., Pellicciotti, F., and Shrestha, A. B.: Glaciers as a Proxy to Quantify the Spatial Distribution of
917 Precipitation in the Hunza Basin, *Mountain Research and Development*, 32, 30–38, 10.1659/mrd-journal-d-11-
918 00097.1, 2012.

919 Immerzeel, W. W., Rutten, M. M., and Droogers, P.: Spatial downscaling of TRMM precipitation using vegetative
920 response on the Iberian Peninsula, *Remote Sensing of Environment*, 113, 362–370, 10.1016/j.rse.2008.10.004, 2009.

921 Juen, M., Mayer, C., Lambrecht, A., Han, H., and Liu, S.: Impact of varying debris cover thickness on ablation: a case
922 study for Koxkar Glacier in the Tien Shan, *The Cryosphere*, 8, 377–386, 10.5194/tc-8-377-2014, 2014.

923 Kääh, A., Berthier, E., Nuth, C., Gardelle, J., and Arnaud, Y.: Contrasting patterns of early twenty-first-century glacier
924 mass change in the Himalayas, *Nature*, 488, 495–498, <https://doi.org/10.1038/nature11324>, 2012.

925 Kumar, A., Negi, H. S., and Kumar, K.: Long-term mass balance modelling (1986–2018) and climate sensitivity of
926 Siachen Glacier, East Karakoram, *Environ Monit Assess*, 192, 368, 10.1007/s10661-020-08323-0, 2020.

927 Lanzhou Institute of Glaciology and Geocryology, C. A. o. S.: Studies and investigations on the Batura Glacier,
928 Karakoram, China Science Publishing & Media Ltd, Beijing1980.

929 Li, S., Yao, T., Yu, W., Yang, W., and Zhu, M.: Energy and mass balance characteristics of the Guliya ice cap in the
930 West Kunlun Mountains, Tibetan Plateau, *Cold Regions Science and Technology*, 159, 71–85,
931 <https://doi.org/10.1016/j.coldregions.2018.12.001>, 2019.

932 Maussion, F., Scherer, D., Mölg, T., Collier, E., Curio, J., and Finkelnburg, R.: Precipitation Seasonality and Variability
933 over the Tibetan Plateau as Resolved by the High Asia Reanalysis, *Journal of Climate*, 27, 1910–1927, 10.1175/jcli-
934 d-13-00282.1, 2014.

935 Mayer, C., Lambrecht, A., Oerter, H., Schwikowski, M., Vuillermoz, E., Frank, N., and Diolaiuti, G.: Accumulation
936 Studies at a High Elevation Glacier Site in Central Karakoram, *Advances in Meteorology*, 2014, 1–12,
937 10.1155/2014/215162, 2014.

938 Mihalcea, C., Mayer, C., Diolaiuti, G., D'agata, C., Smiraglia, C., Lambrecht, A., Vuillermoz, E., and Tartari, G.: Spatial
939 distribution of debris thickness and melting from remote-sensing and meteorological data, at debris-covered
940 Baltoro glacier, Karakoram, Pakistan, *Annals of Glaciology*, 48, 49–57, 2008.

941 Miles, E. S., Pellicciotti, F., Willis, I. C., Steiner, J. F., Buri, P., and Arnold, N. S.: Refined energy-balance modelling of
942 a supraglacial pond, Langtang Khola, Nepal, *Annals of Glaciology*, 57, 29–40, 10.3189/2016AoG71A421, 2016.

943 Miles, E. S., Willis, I., Buri, P., Steiner, J. F., Arnold, N. S., and Pellicciotti, F.: Surface Pond Energy Absorption Across
944 Four Himalayan Glaciers Accounts for 1/8 of Total Catchment Ice Loss, *Geophys Res Lett*, 45, 10464–10473,
945 10.1029/2018GL079678, 2018.

946 Minora, U., Senese, A., Bocchiola, D., Soncini, A., D'agata, C., Ambrosini, R., Mayer, C., Lambrecht, A., Vuillermoz,
947 E., Smiraglia, C., and Diolaiuti, G.: A simple model to evaluate ice melt over the ablation area of glaciers in the
948 Central Karakoram National Park, Pakistan, *Annals of Glaciology*, 56, 202–216, 10.3189/2015AoG70A206, 2015.

949 Mölg, N., Bolch, T., Rastner, P., Strozzi, T., and Paul, F.: A consistent glacier inventory for Karakoram and Pamir
950 derived from Landsat data: distribution of debris cover and mapping challenges, *Earth System Science Data*, 10,
951 1807-1827, 10.5194/essd-10-1807-2018, 2018.

952 Mölg, T., Maussion, F., Yang, W., and Scherer, D.: The footprint of Asian monsoon dynamics in the mass and energy
953 balance of a Tibetan glacier, *The Cryosphere*, 6, 1445-1461, 10.5194/tc-6-1445-2012, 2012.

954 Muhammad, S., Tian, L., Ali, S., Latif, Y., Wazir, M. A., Goheer, M. A., Saifullah, M., Hussain, I., and Shiyin, L.: Thin
955 debris layers do not enhance melting of the Karakoram glaciers, *Sci Total Environ*, 746, 141119,
956 10.1016/j.scitotenv.2020.141119, 2020.

957 Muñoz Sabater, J.: ERA5-Land hourly data from 1981 to present [dataset], 10.24381/cds.e2161bac, 2019.

958 Nicholson, L. and Benn, D. I.: Calculating ice melt beneath a debris layer using meteorological data, *Journal of*
959 *Glaciology*, 52, 463-470, 2006.

960 Nicholson, L. and Stiperski, I.: Comparison of turbulent structures and energy fluxes over exposed and debris-
961 covered glacier ice, *Journal of Glaciology*, 66, 543-555, 10.1017/jog.2020.23, 2020.

962 Nie, Y., Pritchard, H. D., Liu, Q., Hennig, T., Wang, W., Wang, X., Liu, S., Nepal, S., Samyn, D., Hewitt, K., and Chen,
963 X.: Glacial change and hydrological implications in the Himalaya and Karakoram, *Nature Reviews Earth &*
964 *Environment*, 10.1038/s43017-020-00124-w, 2021.

965 Nuimura, T., Fujita, K., and Sakai, A.: Downwasting of the debris-covered area of Lirung Glacier in Langtang Valley,
966 Nepal Himalaya, from 1974 to 2010, *Quaternary International*, 455, 93-101, 10.1016/j.quaint.2017.06.066, 2017.

967 Østrem, G.: Ice Melting under a Thin Layer of Moraine, and the Existence of Ice Cores in Moraine Ridges,
968 *Geografiska Annaler*, 41, 228-230, 10.1080/20014422.1959.11907953, 1959.

969 Rankl, M. and Braun, M.: Glacier elevation and mass changes over the central Karakoram region estimated from
970 TanDEM-X and SRTM/X-SAR digital elevation models, *Annals of Glaciology*, 57, 273-281,
971 10.3189/2016AoG71A024, 2016.

972 Reid, T. D. and Brock, B. W.: An energy-balance model for debris-covered glaciers including heat conduction
973 through the debris layer, *Journal of Glaciology*, 56, 903-916, 2010.

974 Reid, T. D., Carenzo, M., Pellicciotti, F., and Brock, B. W.: Including debris cover effects in a distributed model of
975 glacier ablation, *Journal of Geophysical Research: Atmospheres*, 117, D18105, 10.1029/2012jd017795, 2012.

976 Rounce, D. R., Hock, R., McNabb, R. W., Millan, R., Sommer, C., Braun, M. H., Malz, P., Maussion, F., Mouginot, J.,
977 Seehaus, T. C., and Shean, D. E.: Distributed Global Debris Thickness Estimates Reveal Debris Significantly Impacts
978 Glacier Mass Balance, *Geophys Res Lett*, 48, e2020GL091311, 10.1029/2020GL091311, 2021.

979 Sauter, T., Arndt, A., and Schneider, C.: COSIPY v1.3 – an open-source coupled snowpack and ice surface energy
980 and mass balance model, *Geoscientific Model Development*, 13, 5645-5662, 10.5194/gmd-13-5645-2020, 2020.

981 Shean, D. E., Bhushan, S., Montesano, P., Rounce, D. R., Arendt, A., and Osmanoglu, B.: A Systematic, Regional
982 Assessment of High Mountain Asia Glacier Mass Balance, *Frontiers in Earth Science*, 7,
983 <https://doi.org/10.3389/feart.2019.00363>, 2020.

984 Steiner, J. F., Litt, M., Stigter, E. E., Shea, J., Bierkens, M. F. P., and Immerzeel, W. W.: The Importance of Turbulent
985 Fluxes in the Surface Energy Balance of a Debris-Covered Glacier in the Himalayas, *Frontiers in Earth Science*, 6,
986 10.3389/feart.2018.00144, 2018.

987 Tahir, A. A., Chevallier, P., Arnaud, Y., and Ahmad, B.: Snow cover dynamics and hydrological regime of the Hunza
988 River basin, Karakoram Range, Northern Pakistan, *Hydrology and Earth System Sciences*, 15, 2275-2290,
989 10.5194/hess-15-2275-2011, 2011.

990 Tedesco, M., Lüthje, M., Steffen, K., Steiner, N., Fettweis, X., Willis, I., Bayou, N., and Banwell, A.: Measurement and
991 modeling of ablation of the bottom of supraglacial lakes in western Greenland, *Geophysical Research Letters*, 39,
992 10.1029/2011gl049882, 2012.

993 Wang, X., Tolksdorf, V., Otto, M., and Scherer, D.: WRF-based dynamical downscaling of ERA5 reanalysis data for
994 High Mountain Asia: Towards a new version of the High Asia Refined analysis, *International Journal of Climatology*,
995 41, 743-762, 10.1002/joc.6686, 2020.

996 Winiger, M., Gumpert, M., and Yamout, H.: Karakorum-Hindukush-western Himalaya: assessing high-altitude
997 water resources, *Hydrological Processes*, 19, 2329-2338, 10.1002/hyp.5887, 2005.

998 Wohlfahrt, G., Hammerle, A., Haslwanter, A., Bahn, M., Tappeiner, U., and Cernusca, A.: Disentangling leaf area
999 and environmental effects on the response of the net ecosystem CO₂ exchange to diffuse radiation, *Geophys Res
1000 Lett*, 35, 10.1029/2008gl035090, 2008.

1001 Wohlfahrt, G., Hammerle, A., Niedrist, G., Scholz, K., Tomelleri, E., and Zhao, P.: On the energy balance closure and
1002 net radiation in complex terrain, *Agric For Meteorol*, 226-227, 37-49, 10.1016/j.agrformet.2016.05.012, 2016.

1003 Wortmann, M., Bolch, T., Menz, C., Tong, J., and Krysanova, V.: Comparison and Correction of High-Mountain
1004 Precipitation Data Based on Glacio-Hydrological Modeling in the Tarim River Headwaters (High Asia), *Journal of
1005 Hydrometeorology*, 19, 777-801, 10.1175/jhm-d-17-0106.1, 2018.

1006 Wu, K., Liu, S., Jiang, Z., Liu, Q., Zhu, Y., Yi, Y., Xie, F., Ahmad Tahir, A., and Saifullah, M.: Quantification of glacier
1007 mass budgets in the Karakoram region of Upper Indus Basin during the early twenty-first century, *Journal of
1008 Hydrology*, 603, 10.1016/j.jhydrol.2021.127095, 2021.

1009 Wu, K., Liu, S., Jiang, Z., Zhu, Y., Xie, F., Gao, Y., Yi, Y., Tahir, A. A., and Muhammad, S.: Surging Dynamics of Glaciers
1010 in the Hunza Valley under an Equilibrium Mass State since 1990, *Remote Sensing*, 12, 10.3390/rs12182922, 2020.

1011 Xie, F., Liu, S., Wu, K., Zhu, Y., Gao, Y., Qi, M., Duan, S., Saifullah, M., and Tahir, A. A.: Upward Expansion of Supra-
1012 Glacial Debris Cover in the Hunza Valley, Karakoram, During 1990 ~ 2019, *Frontiers in Earth Science*, 8,
1013 10.3389/feart.2020.00308, 2020.

1014 Xie, F., Liu, S., Gao, Y., Zhu, Y., Bolch, T., Kääb, A., Duan, S., Miao, W., Kang, J., Zhang, Y., Pan, X., Qin, C., Wu, K., Qi,
1015 M., Zhang, X., Yi, Y., Han, F., Yao, X., Liu, Q., Wang, X., Jiang, Z., Shangguan, D., Zhang, Y., Grünwald, R., Adnan, M.,
1016 Karki, J., and Saifullah, M.: Interdecadal glacier inventories in the Karakoram since the 1990s, *Earth System Science
1017 Data*, 15, 847-867, 10.5194/essd-15-847-2023, 2023.

1018 Zemp, M., Huss, M., Thibert, E., Eckert, N., McNabb, R., Huber, J., Barandun, M., Machguth, H., Nussbaumer, S. U.,
1019 Gartner-Roer, I., Thomson, L., Paul, F., Maussion, F., Kutuzov, S., and Cogley, J. G.: Global glacier mass changes
1020 and their contributions to sea-level rise from 1961 to 2016, *Nature*, 568, 382-386, 10.1038/s41586-019-1071-0,
1021 2019.

1022 Zhu, M., Yao, T., Xie, Y., Xu, B., Yang, W., and Yang, S.: Mass balance of Muji Glacier, northeastern Pamir, and its
1023 controlling climate factors, *Journal of Hydrology*, 590, 10.1016/j.jhydrol.2020.125447, 2020.

1024 Zhu, M., Yao, T., Yang, W., Xu, B., Wu, G., and Wang, X.: Differences in mass balance behavior for three glaciers
1025 from different climatic regions on the Tibetan Plateau, *Climate Dynamics*, 50, 3457-3484, 10.1007/s00382-017-
1026 3817-4, 2017.

1027